Received 9 July 2024, accepted 18 August 2024, date of publication 29 August 2024, date of current version 19 September 2024.

Digital Object Identifier 10.1109/ACCESS.2024.3451520

RESEARCH ARTICLE

Seamless Transition Between Microgrid Operation Modes Using ADRC Without an Islanding Detection Algorithm nor PLL

N. YALAOUI, (Member, IEEE), L. DESSAINT, (Life Fellow, IEEE), M. REZA DEHBOZORGI, AND K. AL-HADDAD, (Life Fellow, IEEE)
Department of Electrical Engineering, École de Technologie Supérieure, Montreal, QC H3C 1K3, Canada

Corresponding author: N. Yalaoui (Nabila.yalaoui.1@ens.etsmtl.ca)

This work was supported by the Natural Sciences and Engineering Research Council (NSERC) of Canada.

ABSTRACT The availability and cost of fossil fuels, natural disasters, aging infrastructure, climate change, and rising electricity consumption have affected today's power grids. One of the most practical solutions for achieving green and reliable energy is the use of microgrids. The stability of microgrids dominated by electronic converters presents several challenges. Among the problems encountered are the absence of physical inertia, delay in detecting islanding, and loss of stability associated with the transition between operating modes and variations of the load power. To overcome these challenges, this study presents a new robust control strategy based on active disturbance rejection control (ADRC). It is suitable for both islanded and connected operation modes with a single control, without an islanding detection algorithm or Phase-Locked Loop (PLL). The effectiveness of the control strategy is demonstrated through simulations and a comparative analysis with conventional droop control. Flexibility of the transition is also ensured. The proposed control strategy is successfully validated using a TI C2000 DSP TMS320F28335 microcontroller.

INDEX TERMS Active disturbance rejection control (ADRC), grid-feeding inverter, grid-forming inverter, microgrid, seamless transition, single control.

I. INTRODUCTION

The development of power electronics has led to a high penetration of renewable energy sources into power grids. This has made it possible to reduce the number of synchronous machines and replace them with renewable energy sources interfaced by power inverters. Therefore, the modern power grid is moving towards a system dominated by inverters rather than rotary generators. While this is economically and environmentally beneficial, power from a non-synchronous renewable energy source does not provide any inertia [1]. As renewable energy sources begin to replace the synchronous machines that help the power system to resist to frequency deviations, the system's ability is decreasing. The reduced inertia in the system results in a high rate-of-change-of-frequency (ROCOF) and a low frequency nadir (minimum frequency point) after a disturbance [2]. Since the stability and reliability of the system are threatened, many efforts should therefore be devoted to improve the inertia of the system. Several studies have demonstrated that the frequency stability is a major concern for electricity system operators due to inertia [3], [4], [5], [6], [7]. Therefore, a fast and efficient controller is needed. Since power converters allow to act quickly [8] and its characteristics are defined by its control algorithms, grid-forming inverters (GFMs) are considered a safe and reliable technology for low-inertia grids [9]. The control strategies developed are based on the imitation of the characteristics of a synchronous machine.

The control of the inverter plays a critical role in the robust operation of the microgrids. Two major control strategies have been proposed to achieve seamless transfer from one mode of operation to another. The first strategy is a hybrid control, in which two controllers are used. The inverter is controlled as a power source in the grid-connected mode and as a voltage source in the islanded mode. An islanding detection system is required to trigger or change the operation

The associate editor coordinating the review of this manuscript and approving it for publication was Shafiqul Islam.

© 2024 The Authors. This work is licensed under a Creative Commons Attribution 4.0 License.
For more information, see https://creativecommons.org/licenses/by/4.0/

mode [10], [11], [12]. In addition to design and tuning difficulties, the use of two controllers increases system costs and causes considerable transient effects, including delays and significant overruns of the PCC voltage and frequency [13] and [14]. The second strategy is based on a single controller operating in both connected and islanded modes: [15], [16], [17], [18], [19], [20], [21]. However, these controllers are mathematically complex and difficult to implement. Droop control is used first in uninterruptible power supply (UPS) systems [22]. Several improvements to this strategy have been reported, as in [15], [17], [23], and [24]. Although this control has shown good performance, the lack of inertia usually limits its applications. Other researchers have proposed commands based on emulating the behavior of synchronous generators under the name of virtual synchronous machine (VSM) [25]. This control combines the advantages of the inverter and the synchronous machine. Due to the poor voltage quality during island mode, several VSM enhancements have been proposed in [26] and [27]. As in [21], the authors used the adaptive control based on an artificial neural network of a VSM. They get a good steady-state response. But its performance is mediocre under dynamic conditions and the transition between the two modes of operation is not addressed. In addition, the VSM parameters are predicted by a neural network, which is a complex process. Another strategy based on the principle of emulation of the electromechanical behavior of the synchronous generator is presented in [18]. However, this control is difficult to implement due to its mathematical complexity. When switching from one mode to another, the frequency stabilizes after a long time with significant overshoots. The researchers of [20] used a robust linear quadratic nested loop regulator and a mixed H2/H∞ controller to ensure the operation of a microgrid. This depends on a PLL and an islanding detection algorithm and is difficult to implement. A cascade control strategy is proposed in [21]. The outer loop is VSM-based, and the internal voltage and current control loops use sliding mode control (SMC). This improves accuracy, but the transitional time and the overcoming are important. This approach is difficult to implement and presents a chatter phenomenon that can lead to controller instability. A summary of existing control schemes and their restrictions is presented in Table 1.

Some of these methods require an islanding detection algorithm to generate controller references according to the microgrid operating mode. During the interval between the occurrence of a main grid failure and the detection of islanding, the PCC voltage is neither controlled by the main grid nor by the inverter. Therefore, the use of an islanding detection algorithm renders the quality of the PCC voltage highly dependent on the speed and accuracy of the islanding detection method. Designing a reliable, accurate, and fast detection algorithm is challenging. This can generate a false trigger signal or cause a no-detection zone. If islanding occurs but has not yet been detected, and the control structure remains constant, undesirable transients may result [28].

Several synchronization algorithms have been proposed in the literature and applied in several controllers. They can be classified into open-loop and closed-loop algorithms. Open-loop algorithms can easily detect the amplitude, phase, and frequency of an input signal.

The Kalman filter [29], discrete Fourier transform [30], zero-crossing detection, [31] and artificial Intelligence [32] are common examples of synchronization algorithm. In contrast, closed-loop systems use an adaptive control loop to estimate grid parameters. Among these algorithms are the PLL [33], the frequency-locked loops (FLL) [34] and the delayed signal cancellations [35]. The PLL is simple, efficient, and robust, and it is the most widely used in several

TABLE 1. Summary of literature review.

Ref.	Control technique	Islanding detection	Synchronisation	Sensors	Frequency control	Remarks
[15], [23]	Droop control, 2024	Yes	PLL	3	Low	-Complex to implement. -Slow transient response.
[17]	Droop control with virtual impedance (DVI), 2023	Yes	MSOGI-FLL	3	Low	-Slow detection speed and reliability -Significant frequency deviation in islanded mode
[18]	Virtual synchronizing torque, 2024	No	No	2	Mediocre	-Expensive and complex to implement -Slow transient response with significant overshoots
[19]	Adaptive neural network, 2021	No	VSG	2	Mediocre	-Expensive and complex to implement -Control effect greatly depends on model accuracy
[20]	Linear quadratic regulator, 2022	yes	PLL	4	Good	-Expensive and complex implementation. -Control effect greatly depends on model accuracy
[21]	Sliding control, 2022	No	VSG	5	Mediocre	-Expensive and complex implementation. -Produces the chattering phenomenon in control.
Proposed control	**ADRC control**	**No**	**No**	**2**	**Better**	**-Easy to implement** **-fast dynamics**

applications such as control and communication systems. It allows synchronization of its output signal with the reference input signal. However, several disruptions have negative impacts and affect the tracking ability of the PLL. Therefore, various changes and improvements have been made in recent years. They help to ensure reliable operation with better stability and faster synchronization. These synchronization algorithms include the synchronous frame of reference PLL (SRF-PLL), generalized dual integrator second-order PLL (DSOGI-PLL), synchronous dual frame of reference PLL (DSRF-PLL), and enhanced PLL (EPLL).

Several islanding detection algorithms have been evaluated [36], [37] and the risk of instability has increased. PLLs are difficult to implement owing to their nonlinear properties and complex configuration [38]. All synchronization algorithms mentioned above have limitations and drawbacks that need to be considered [39]. Controls without PLL are preferred to avoid stability issues [40].

The use of islanding detection and synchronization algorithms renders the system less reliable and complex. In addition to design and tuning difficulties, using two controllers increases the system costs and causes considerable transient effects, including delays, large overshoots, and undershoots in the PCC voltage and frequency [13], [14]. Therefore, the use of a control strategy that does not require an islanding detection and synchronization algorithms is very attractive. This increases the flexibility, resilience, and reliability of the microgrid.

In recent years, control technology known as Active Disturbance Rejection Control (ADRC) has been explored in almost all areas of control engineering as an alternative to conventional proportional-integral-derivative (PID) controllers and modern model-based controls [41], [42].

The basic idea of ADRC is to estimate the unknown system dynamics and external perturbation using an Extended State Observer (ESO) and then compensate for the total perturbation in the control law. Therefore, it is not necessary to determine the exact model for the control system. Reference [43] introduced a third-order ADRC grid-connected inverter controller with an enhanced observer to improve power quality. In [44], a third-order ADRC controller is designed to realize the current decoupling control of the inverter in the connected mode. In [45], a second-order ADRC is adopted as the current inner-loop controller of the inverter to realize the transition between two controllers, one for the connected mode and the other for the islanded mode. This strategy is based on a phase-locked loop (PLL) to synchronize the PCC voltage. Most control methods cited in the literature require several measurement sensors, which reduces their reliability.

The objective of this study is to develop a robust and simple controller for a three-phase inverter with a seamless transition between the two operating modes. A linear ADRC design method is proposed and applied to reduce model complexity and controller computational load. It can treat the overall disturbance using a cascade-integral model and an extended state observer (ESO). This only requires measurements of the grid voltage and inverter output. Capacitor, grid, and inverter current sensors are not required.

The main contributions of the proposed control are:

- Ensure a smooth transition between grid connected and islanded modes without control reconfiguration.
- Increase the reliability of the microgrid by using a single scheme with fewer sensors.
- No requirement of an islanding detection and synchronization algorithms.
- Precise regulation of the voltage and frequency of the microgrid in the islanded mode.
- A good dynamic response under load variations and during the transition from one operating mode to another is observed, unlike some methods that have slow transient responses and significant overshoots.

The remainder of this paper is organized as follows. Section II describes the mathematical theory of active disturbance rejection control. Section III details the proposed control based on the ADRC. Section IV presents a stability analysis and parameter tuning of the proposed control. The simulation results in Section V confirm the effectiveness of the proposed method in comparison with the traditional droop controller (DVI). Section VI presents an experimental validation of the proposed ADRC using a real-time implementation. Finally, Section VII concludes the paper.

II. MATHEMATICAL THEORY OF ACTIVE DISTURBANCE REJECTION CONTROL

The n-order ADRC configuration is illustrated in Fig.1. It contains three main elements: a tracking differentiator (TD), extended state observer (ESO), and state error feedback (SEF). The TD generates a transition process for the system. It is used to extract the derivatives of the reference signal and to use them as a reference profile. The ESO is the central component of the control group. This information is used to process and estimate the total disturbance. The SEF uses the estimated disturbance to generate a control signal with the objective of rapidly compensating for the disturbance. The total disturbance is compensated for in real-time, which significantly improves the robustness and reliability of the system [41].

Several methods can be used to generate the derivatives of the TD component reference signal. The general form of this equation is as follows:

$$\begin{cases} \dot{V}_1 = V_2 \\ \dot{V}_2 = V_3 \\ . \\ . \\ . \\ \dot{V}_{n-1} = V_n \\ \dot{V}_n = \lambda^n f(V_1 - r, \dfrac{V_2}{\lambda}, \ldots, \dfrac{V_n}{\lambda^{n-1}}) \end{cases} \tag{1}$$

r is the input signal. V_i $(i = 1, 2 \ldots n)$ are the outputs. λ is the convergence speed factor for control. $f(V_1 - r, \frac{V_2}{\lambda}, \ldots, \frac{V_n}{\lambda^{n-1}})$ guarantees rapid convergence of V_1 to r.

The ESO uses the output signal y and control signal u as inputs. The estimated values of the state variables and disturbances are the outputs. It is designed in the following form:

$$\begin{cases} e = Z_1 - y \\ \dot{Z}_1 = Z_2 - \beta_{o1} f_1(e) \\ \dot{Z}_2 = Z_3 - \beta_{o2} f_2(e) \\ . \\ . \\ . \\ \dot{Z}_n = Z_{n+1} - \beta_{on} f_n(e) + b_0 u \\ \dot{Z}_{n+1} = -\beta_{o(n+1)} f_{(n+1)}(e) \end{cases} \tag{2}$$

β_{oj} ($j = 1, 2, \ldots.$) are the observer gains. $f_j(e) = \text{fun}\left(e, \alpha_{0j}, \delta_{0j}\right)$. e is the observer error.

SEF is used to limit the residual error and achieve the desired control objective. The control signal is designed as follows:

$$u = u_0 - \frac{Z_{n+1}}{b_0}$$
$$u_0 = \sum_{i=1}^{n} \beta_i \text{fun}(e_i, \alpha_j', \delta_i') \tag{3}$$

$\beta_i (i = 1, 2, \ldots, n)$ are controller gains and e_i denotes the controller error.

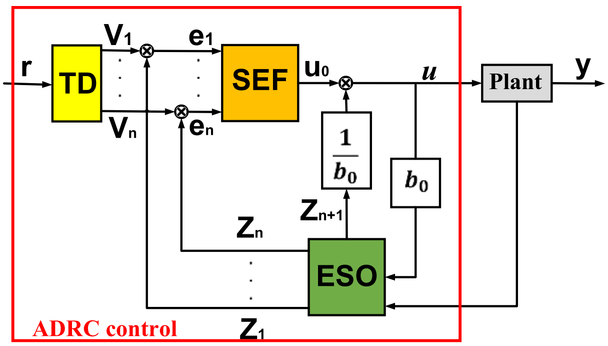

FIGURE 1. Block-diagram of the ADRC controller.

$\text{fun}\left(e, \alpha_{0j}, \delta_{0j}\right)$ and $\text{fun}\left(e_i, \alpha_j', \delta_i'\right)$ are nonlinear functions defined as follows:

$$f_j(e_i) = \text{fun}\left(e_i, \alpha_{0j}, \delta_{0j}\right) = \begin{cases} \dfrac{e_i}{\delta_{0j}^{1-\alpha_{0j}}} & \text{if } |e_i| \le \delta_{0j} \\ |e_i|^{\alpha_{0j}} \text{sgn}(e_i) & \text{if } |e_i| > \delta_{0j} \end{cases} \tag{4}$$

$(\alpha_{0j}, \delta_{0j})$ are constants. $\text{sgn}(e_i)$ is the sign function. $\alpha_{0j} < 1$, When α_{0j} is equal to 1, the function $f_j(e) = e$. It becomes a linear function, and the control is a linear ADRC. Its main benefit is that the parameter settling is simpler, and the control effect is relatively soft.

A linear ADRC design method is adopted and applied in this study to reduce the complexity of the model and the computation of the controller.

III. PROPOSED CONTROL STRATEGY BASED ON ADRC

The system studied herein (Fig.2) consists of a three-phase insulated-gate bipolar transistor (IGBT) inverter bridge, an inverter DC power source, a main grid, resistors and inductors equivalent on the inverter and main grid sides, and a local load.

Applying Kirchhoff's current and voltage laws, the equations that describe the dynamic behavior of this converter are:

$$\begin{cases} \dfrac{dv_c}{dt} = i_C = \dfrac{1}{C}(i_{inv} - i_G) \\ \dfrac{di_{inv}}{dt} = \dfrac{1}{L}(v_{inv} - v_c - Ri_{inv}) \\ \dfrac{di_G}{dt} = \dfrac{1}{L_G}(v_c - v_G - R_G i_G) \end{cases} \tag{5}$$

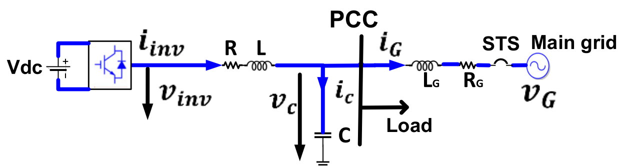

FIGURE 2. Block-diagram of the inverter connected to the main grid.

R and L are the equivalent resistance and inductance of the inverter side. R_G and L_G are the equivalent resistance and inductance on the grid side, respectively. v_{inv}, v_c an v_G are the inverter output, PCC, and main grid voltages, respectively. i_G, i_C and i_{inv} are the currents injected into the main grid, capacitor, and inverter, respectively.

The PCC voltage control must be maintained in the connected mode to ensure load supply even during unexpected grid outages. Hence, the choice of the state variable vector is $x = [x_1 x_2 x_3] = [v_c i_{inv} i_G]$.

In this case, the system of (5) becomes:

$$\begin{cases} \dot{x_1} = k_3 x_2 - k_3 x_3 \\ \dot{x_2} = -k_4 x_1 - k_5 x_2 + k_4 v_{inv} \\ \dot{x_3} = k_2 x_1 - k_1 x_3 - k_2 v_G \end{cases}$$
$$k_1 = \frac{R_G}{L_G}, k_2 = \frac{1}{L_G}, k_3 = \frac{1}{C}, k_4 = \frac{1}{L}, k_5 = \frac{R}{L} \tag{6}$$

We take variables $(\overline{x_1}, \overline{x_2}, \overline{x_3})$ equal to the voltage v_c, their first and second derivatives $\dot{v}_c$ and $\ddot{v}_c$, respectively. In this case, we can write the cascade integral [43] as:

$$\begin{cases} \dot{\overline{x_1}} = \overline{x_2} \\ \dot{\overline{x_2}} = \overline{x_3} \\ \dot{\overline{x_3}} = f(\overline{x_1}, \overline{x_2}, \overline{x_3}, v_G) + k_1 k_3 k_4 v_{inv} \end{cases} \tag{7}$$

where:

$$\begin{cases} f\left(\overline{x_1},\overline{x_2},\overline{x_3},v_G\right)=\alpha_1\overline{x_1}+\alpha_2\overline{x_2}+\alpha_3\overline{x_3}+ \\ k_2k_3k_5v_G+k_3k_4\dot{v}_{inv}+k_2k_3\dot{v}_G \\ \alpha_1=-k_2k_3k_5-k_1k_3k_4 \\ \alpha_2=-\left[k_1k_5+k_2k_3+k_3k_4\right] \\ \alpha_3=-\left[k_1+k_5\right] \end{cases} \tag{8}$$

The function $f\left(\overline{x_1},\overline{x_2},\overline{x_3},v_G\right)$ depend on the voltage at the output of the inverter v_{inv} and that of the main grid v_G. This makes it possible to monitor voltage disturbances.

The relation between v_{inv} and the control signal v_{pwm} is:

$$v_{inv}=v_{pwm}\mathrm{Vdc} \tag{9}$$

Replacing (9) in (7), we get:

$$\begin{cases} \dot{\overline{x_1}}=\overline{x_2} \\ \dot{\overline{x_2}}=\overline{x_3} \\ \dot{\overline{x_3}}=f\left(\overline{x_1},\overline{x_2},\overline{x_3},v_G\right)+b_0v_{pwm} \end{cases} \tag{10}$$

Coefficient b_0 describes the influence of the control variable on the cascade integral system. It is equal to $b_0=k_1k_3k_4\mathrm{Vdc}$.

We consider the transition between the operating modes of the microgrid, modeling, and measurement errors to be inevitable external disturbances in the microgrid. Therefore, we must add an extended variable $\overline{x_4}$ in (10) to represent the external disturbances as follows:

$$\begin{cases} \dot{\overline{x_1}}=\overline{x_2} \\ \dot{\overline{x_2}}=\overline{x_3} \\ \dot{\overline{x_3}}=f\left(\overline{x_1},\overline{x_2},\overline{x_3},v_G\right)+\overline{x_4}+b_0v_{pwm} \end{cases} \tag{11}$$

For a third-order system, a fouth-order ESO should be used because global disturbance is treated as an additional state variable. The observer used in this application has the following form:

$$\begin{cases} e_{o1}=Z_1-\overline{x_1} \\ \dot{Z}_1=Z_2-b_1e_{o1} \\ \dot{Z}_2=Z_3-b_2e_{o1} \\ \dot{Z}_3=f\left(Z_1,Z_2,Z_3,v_G\right)+Z_4-b_3e_{o1} \\ +b_0v_{pwm} \\ \dot{Z}_4=-b_4e_{o1} \\ P_{estim}=\left(f\left(\overline{x_1},\overline{x_2},\overline{x_3},v_G\right)+Z_4\right)/b_0 \end{cases} \tag{12}$$

e_{o1} is the estimation error. It is between the measured voltage v_c and its estimated value. $[Z_1, Z_2, Z_3, Z_4]$ are the estimations of $\overline{x_1}, \overline{x_2}, \overline{x_3}$ and the external disturbance $\overline{x_4}$, respectively. P_{estim} represents global disturbance estimation. b_1, b_2, b_3 and b_4 are the parameters of the ESO.

Since ESO creates the opportunity to eliminate the influence of disturbance, the estimated values $[Z_1, Z_2, Z_3]$ tend towards their references $[{v_c}^*, \dot{v}_c^*, \ddot{v}_c^*]$, respectively. In this case, the errors e_1, e_2 and e_3 converge to zero (13).

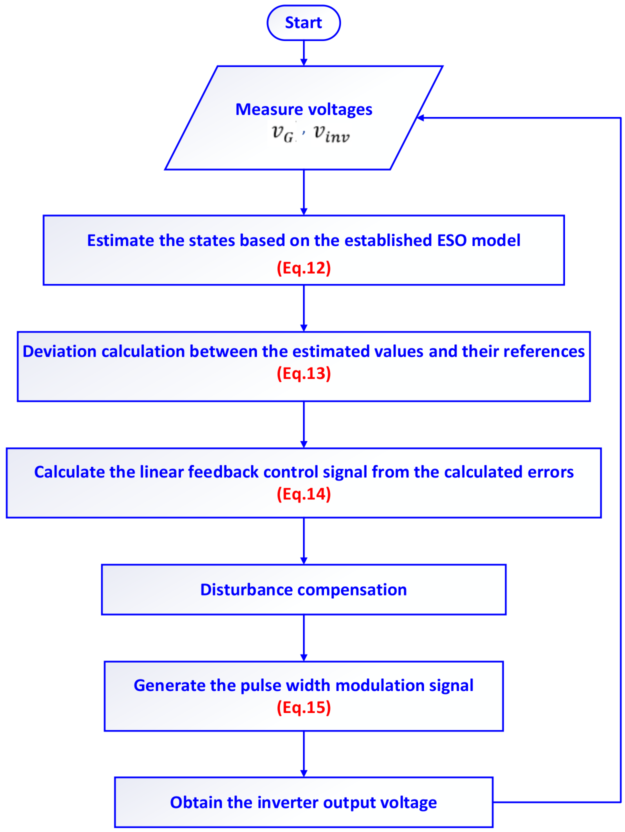

FIGURE 3. Flowchart of the proposed ADRC algorithm.

$$\begin{cases} e_1={v_c}^*-Z_1 \\ e_2=\dot{v}_c^*-Z_2 \\ e_3=\ddot{v}_c^*-Z_3 \end{cases} \tag{13}$$

The expression of the control law used by the component SEF is:

$$u_0=\beta_1e_1+\beta_2e_2+\beta_3e_3 \tag{14}$$

$\boldsymbol{v_c}^*$ is the reference voltage. This is used by the tracking differentiator to obtain the first and second derivatives $\dot{v}_c^*$ and $\ddot{v}_c^*$, respectively.

β_1, β_2 and β_3 are the coefficients that need to be adjusted to improve control performance.

The total disturbance is compensated to determine the control law v_{pwm} as follows:

$$v_{pwm}=u_0-\frac{P_{estim}}{b_0} \tag{15}$$

A flowchart of the algorithm is given in Fig. 3 to further explain the mechanism of the proposed controller and the proposed control scheme is shown in Fig. 4.

The voltages v_{inv} and v_G must be measured and used as inputs to the ESO. Then, the designed ESO can estimate the variables $[Z_1, Z_2, Z_3, Z_4]$ at the output. After that, the errors between $[{v_c}^*, \dot{v}_c^*, \ddot{v}_c^*]$ and $[Z_1, Z_2, Z_3]$ are combined

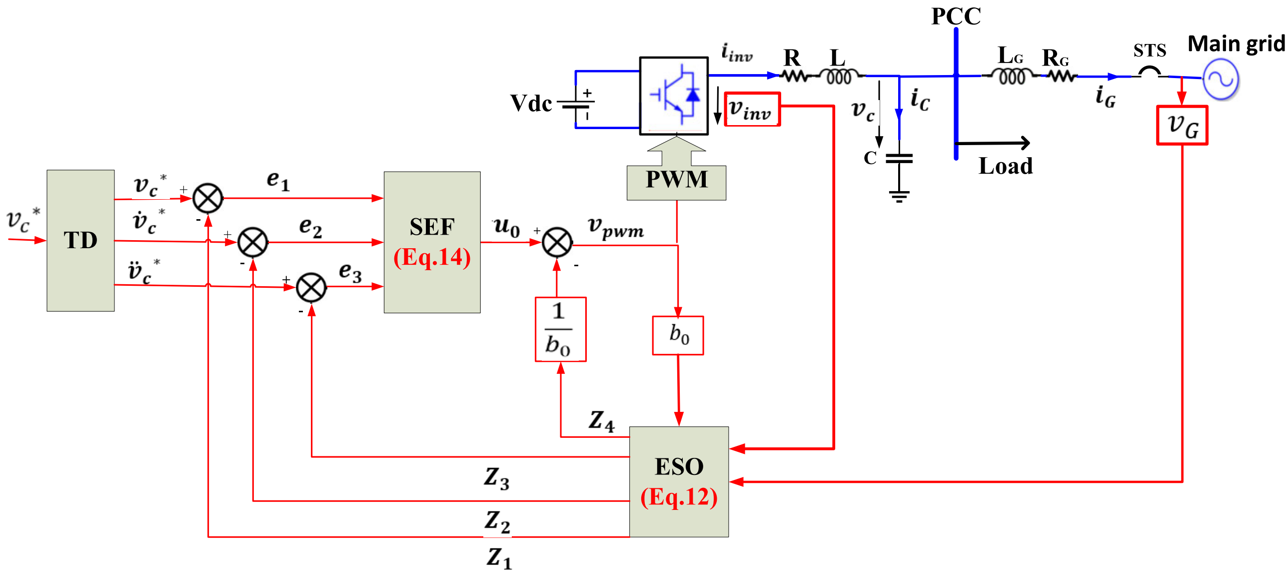

FIGURE 4. Proposed control scheme.

to obtain the control signal u_0. The signal v_{pwm} is obtained after compensation of the disturbance. Finally, v_{pwm} generates pulse width modulation signals for the three-phase inverter.

IV. STABILITY ANALYSIS AND PARAMETERS TUNING

The ESO and SEF settings have a significant impact on the controller performance. The parameters of each control unit can be designed individually, based on the separation principle.

A. THE ESO STABILITY

According to (12), we can write the estimation errors as follows:

$$\begin{cases} e_{o1} = Z_1 - \overline{x_1} \\ e_{o2} = Z_2 - \overline{x_2} \\ e_{o3} = Z_3 - \overline{x_3} \\ e_{o4} = Z_4 - \overline{x_4} \end{cases} \tag{16}$$

The derivative of e_{o1}, e_{o2}, and e_{o3} are:

$$\begin{cases} \dot{e}_{o1} = \dot{Z}_1 - (\dot{\overline{x_1}}) \\ \dot{e}_{o2} = \dot{Z}_2 - (\dot{\overline{x_2}}) \\ \dot{e}_{o3} = \dot{Z}_3 - (\dot{\overline{x_3}}) \end{cases} \tag{17}$$

After simplification, we have:

$$\begin{cases} \dot{e}_{o1} = e_{o2} - b_1 e_{o1} \\ \dot{e}_{o2} = e_{o3} - b_2 e_{o1} \\ \dot{e}_{o3} = e_{o4} + \alpha_1 e_{o1} + \alpha_2 e_{o2} + \alpha_3 e_{o3} - b_3 e_{o1} \end{cases} \tag{18}$$

The characteristic equation of ESO, $\lambda_0(s)$ is:

$$\lambda_0(s) = s^4 + (b_1 - \alpha_3)s^3 + (b_2 - \alpha_2 - b_1\alpha_3)\,s^2 + (b_3 - \alpha_1 - b_1\alpha_2 - b_2\alpha_3)\,s + b_4 \tag{19}$$

The roots of (19) are defined using the pole configuration method [46], where the poles are at $(-\omega_0)$. ω_0 is the observer bandwidth. So, we can write:

$$s^4 + (b_1 - \alpha_3)s^3 + (b_2 - \alpha_2 - b_1\alpha_3)\,s^2 + (b_3 - \alpha_1 - b_1\alpha_2 - b_2\alpha_3)\,s + b_4 = (s + \omega_0)^4 \tag{20}$$

We will have:

$$\begin{cases} b_1 = 4\omega_0 + \alpha_3 \\ b_2 = 6\omega_0^2 + \alpha_2 + b_1\alpha_3 \\ b_3 = 4\omega_0^3 + \alpha_1 + b_1\alpha_2 + b_2\alpha_3 \\ b_4 = \omega_0^4 \end{cases} \tag{21}$$

The design of the ESO parameters plays a more important role in the stability of the microgrid. The necessary and sufficient conditions for the stability by the Routh Hurwitz criterion are:

1. All coefficients of the characteristic equation must be nonzero and have the same sign.
   The coefficients of (19) are:

$$\begin{cases} a_0 = 1 \\ a_1 = b_1 - \alpha_3 \\ a_2 = b_2 - \alpha_2 - b_1\alpha_3 \\ a_3 = b_3 - \alpha_1 - b_1\alpha_2 - b_2\alpha_3 \\ a_4 = b_4 \end{cases} \tag{22}$$

   According to (8), the coefficients α_1, α_2 and α_3 are negative. As ω_0 is greater than zero, it is easy to see that the coefficients in (21) and (22) are all positive.
2. The Routh determinant Δ must be positive.

$$\Delta = (a_1 a_2 - a_0 a_3)a_3 - a_1^2 a_4 > 0 \tag{23}$$

We replace (22) in (23), we will have:

$$\Delta = ((b_1-\alpha_3)(b_2-\alpha_2 - b_1\alpha_3) - (b_3-\alpha_1-b_1\alpha_2 - b_2\alpha_3))$$
$$(b_3 - \alpha_1 - b_1\alpha_2 - b_2\alpha_3) - (b_1 - \alpha_3)^2 b_4 \quad (24)$$

Because the bandwidth ω_0 is positive, $\Delta > 0$ is ensured and the ESO is stable.

B. CONTROLLER STABILITY AND ERROR ANALYSIS

The expression (14) can be written in S-domain:

$$u_0 = (\beta_1 + \beta_2 s + \beta_3 s^2)v_c{}^* - \beta_1 Z_1 - \beta_2 Z_2 - \beta_3 Z_3 \quad (25)$$

Replacing the S-domain description of (12) in (25), we obtain

$$\overline{x_1} = G_c(s)v_c{}^* + G_e(s)e_{01} \quad (26)$$

where:

$$G_c(s) = \frac{b_0\left(\beta_1 + \beta_2 s + \beta_3 s^2\right)}{\left(b_0\beta_1 + b_0\beta_2 s + b_0\beta_3 s^2 + s^3\right)} \quad (27)$$

$$G_e(s) = \frac{D(s)}{\left(b_0\beta_1 + b_0\beta_2 s + b_0\beta_3 s^2 + s^3\right)} \quad (28)$$

$D(s) = -s^3 - (b_1 + b_0\beta_3)s^2 - \left(b_2 + b_0\beta_2 b_1 + b_0\beta_3 b_1\right)s - b_0\beta_2 b_1 - b_0\beta_3 b_2 - b_3$. $G_c(s)$ is the tracking term and $G_e(s)$ is a disturbance term. The estimation error e_{01} of ESO is primarily related to $G_e(s)$. When e_{o1} converged to zero, the disturbance term disappeared. The variable follows the reference quickly without any overshoot, and the transfer function between $\overline{x_1}$ and the reference $v_c{}^*$ is

$$\frac{\overline{x_1}}{v_c^*} = \frac{b_0\left(\beta_1 + \beta_2 s + \beta_3 s^2\right)}{\left(b_0\beta_1 + b_0\beta_2 s + b_0\beta_3 s^2 + s^3\right)} \quad (29)$$

According to the stability theory, the roots of the characteristic equation of (29) must be negative real numbers, so that the estimated variables converge in a finite period towards the desired variables. Therefore, a stable controller can be obtained only by determining the appropriate values of β_1, β_2 and β_3.

The control parameters can be determined using the control bandwidth ω_c. By placing all poles at $(-\omega_c)$, the characteristic polynomial of (29) can be rewritten as

$$\lambda(s) = \left(s^3 + b_0\beta_1 + b_0\beta_2 s + b_0\beta_3 s^2\right) = (s+\omega_c)^3 \quad (30)$$

Thus,

$$\begin{cases} \beta_1 = \dfrac{\omega_c^3}{b_0} \\ \beta_2 = 3\dfrac{\omega_c^2}{b_0} \\ \beta_3 = 3\dfrac{\omega_c}{b_0} \end{cases} \quad (31)$$

Obviously, the SEF is stable because all roots of the characteristic polynomial are in the left plane [46].

C. IMPACT OF ESO AND SEF BANDWIDTH ON SYSTEM PERFORMANCE

We replace (31) in (29) and we will have the transfer function between $\overline{x_1}$ and its reference v_c^* as a function of ω_c, Therefore, (29) becomes:

$$tf_c(s) = \frac{\overline{x_1}}{v_c^*} = \frac{\omega_c^3 + 3\omega_c^2 s + 3\omega_c s^2}{\omega_c^3 + 3\omega_c^2 s + 3\omega_c s^2 + s^3} \quad (32)$$

Let $\omega_c = (500, 1000, 3000, 5000, 8000)$ rad/s, the Bode diagram of $tf_c(s)$ is shown in Fig. 5. We notice that the controlled voltage follows the reference very well with the increase of ω_c. Furthermore, with the increase of ω_c, the estimation error will be reduced.

The transfer function between disturbance estimation error e_{o4} and the external disturbance $\overline{x_4}$ is determined from equation system (18). It is written as follows:

$$tf(s) = \frac{e_{o4}}{\overline{x_4}} = \frac{s^4 + b_1 s^3 + b_2 s^2 + b_3 s}{\lambda_0(s)} \quad (33)$$

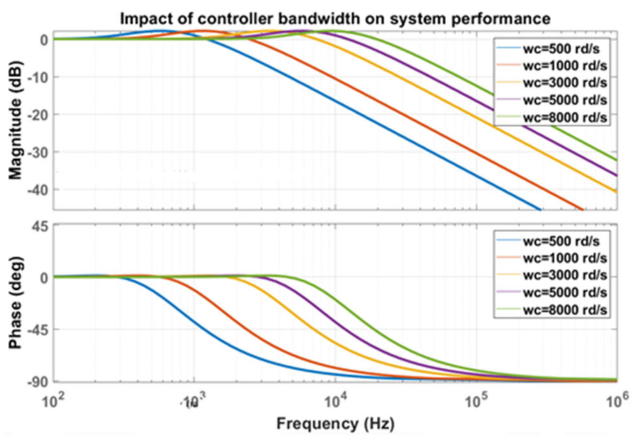

FIGURE 5. Impact of controller bandwidth on system performance.

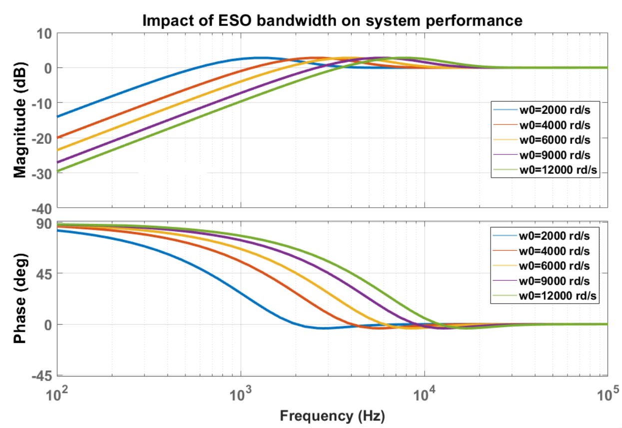

FIGURE 6. Impact of ESO bandwidth on system performance.

We replace b_1, b_2 and b_3 by their expressions in (21), we will have:

$$tf(s) = \frac{s^4 + 4\omega_0 s^3 + 6\omega_0^2 s^2 + 4\omega_0^3 s}{(s+\omega_0)^4} \quad (34)$$

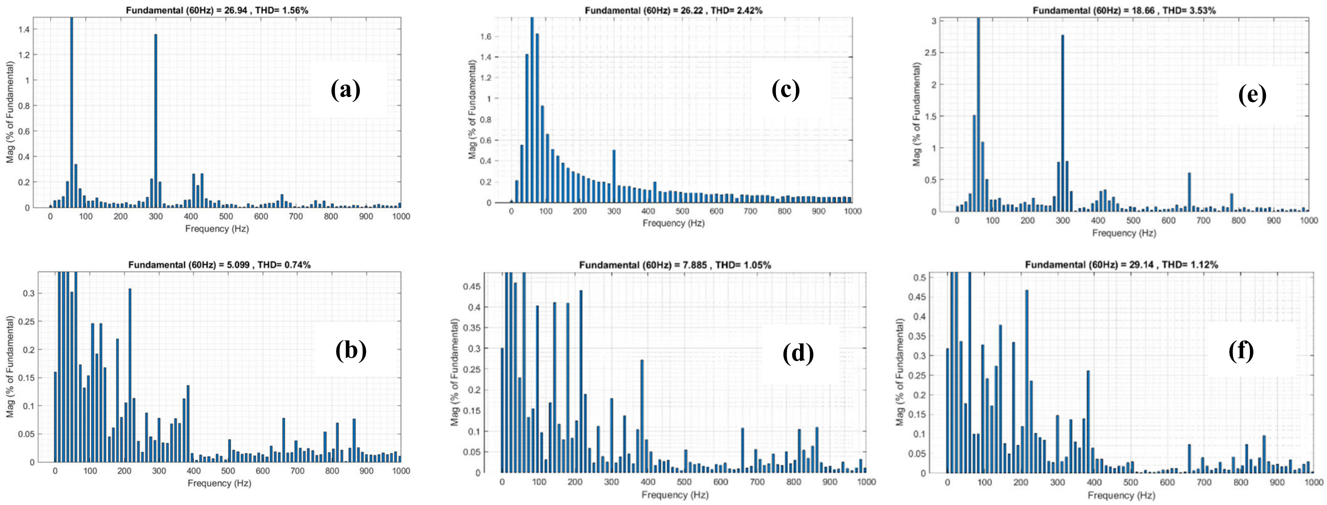

FIGURE 7. Grid current THD during connected mode. (a) and (b) $L_G = 10mH$. (c) and (d) for $LG = 4mH$. (e) and (f) for $LG = 100\mu H$. (a), (c) and (e) with DVI control. (b), (d) and (f) with ADRC control.

TABLE 2. System parameters used for simulation.

Description	Value	Unit
DC bus voltage Vdc	400	V
Grid voltage V_G	120	V
Grid-side inductance L_G	4	mH
Grid-side resistance R_G	0.095	Ω
Inverter-side inductance L	1.2	mH
Inverter-side resistance R	0.11	Ω
Capacitance C	60	µF
Frequency f	60	Hz

TABLE 3. Parameters of the ESO and SEF.

Description	Value	Unit
Controller bandwidth ω_c	3000	rd/s
ESO Bandwidth ω_0	9685	rd/s
Sampling time interval	50	µs

TABLE 4. The THD values of i_G under L_G variation.

L_G	**10 mH**	**4 mH**	**100μH**
ADRC	0.74%	1.05%	1.12%
DVI	1.56%	2.42%	3.53%

Fig.6 shows the amplitude–frequency characteristics of the tf (s) to estimation error with ω_0 sweeping from 2000 rad/s to 12000 rad/s. As ω_0 increases, the ability to suppress the disturbances of the control system is enhanced, which means that the ESO can obtain more accurate estimation results. However, the increase of ω_0 is also limited by measurement noise sensitivity [47]. A trade-off can be made with the balance between tracking performance and smooth transition of the control signal.

To summarize the design steps of the observer and controller, a coherent design and optimization procedure of the proposed ADRC is given as follows [47]:

Step 1: Model the system mathematically and define the parameter b_0 as equal to $k_1k_3k_4$Vdc. Then, select design parameters ω_0 and ω_c).

Step 2: Implement an ESO providing the estimates of the controlled voltage, their derivatives and the total disturbance. Then, construct the SEF control law.

Step 3: Define ω_0 and ω_c and simulate the system. It should be noted that the observer's gains must be chosen considering the speed of estimation of the state and the sensitivity to noise and disturbances.

Furthermore, it is mandatory to consider that the inner loop is faster than the outer loop when adjusting the parameters of the observer and the control law. A common rule of thumb is used to choose the controller bandwidth [47]: $\omega_c = (1/10 \sim 1/2)\omega_0$.

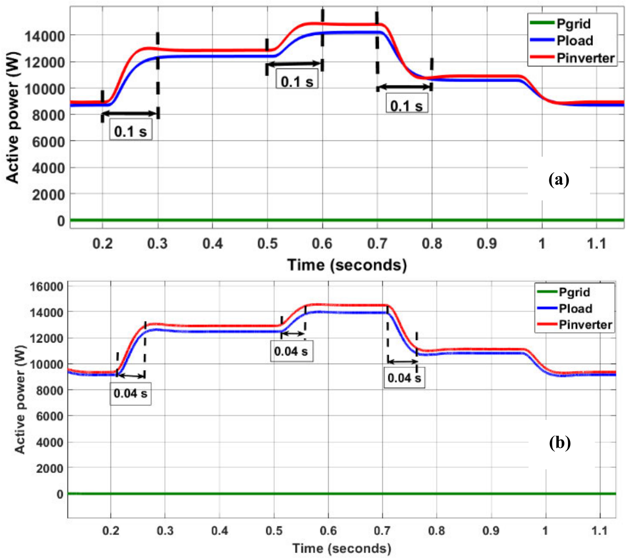

FIGURE 8. Active power during islanded mode. (a) with DVI control. (b) with ADRC control.

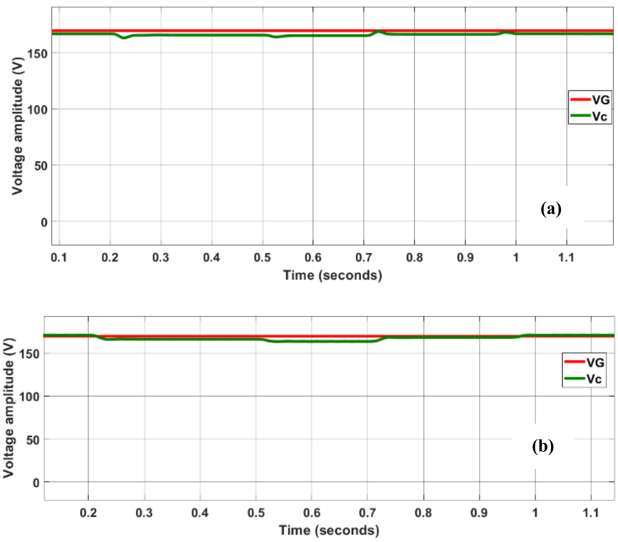

FIGURE 10. PCC voltage amplitude during islanded mode. (a) with DVI control. (b) with ADRC control.

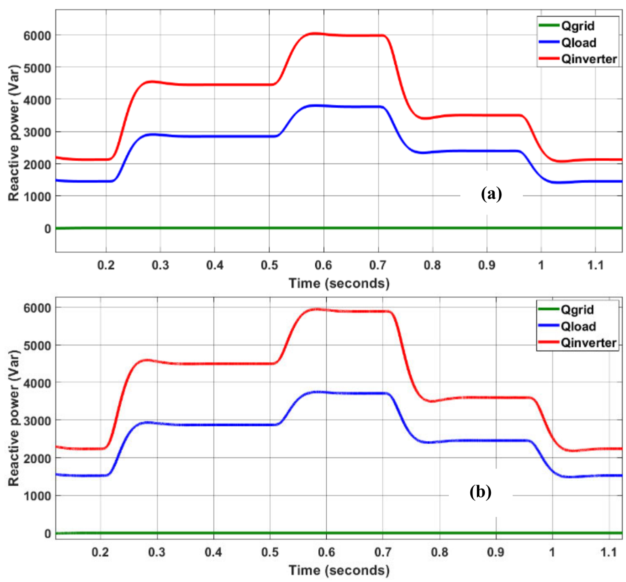

FIGURE 9. Reactive power during islanded mode. (a) with DVI control. (b) with ADRC control.

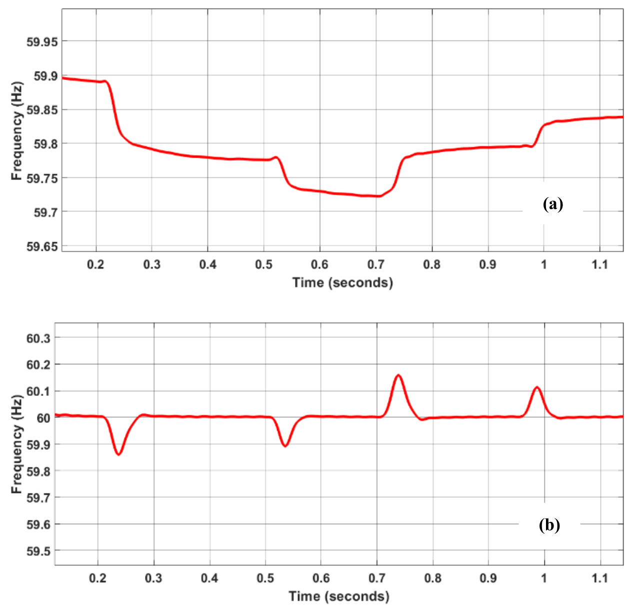

FIGURE 11. Frequency variation during islanded mode. (a) with DVI control. (b) with ADRC control.

Step 4: Gradually increase ω_0 and keep ω_c constant until the voltage and its derivatives follow their references.

The optimal values of ω_0 and ω_c are determined taking into account the stability, the transient performances, and the suppression of noise and oscillations of the system.

V. COMPARATIVE ANALYSIS OF ADRC PROPOSED WITH DVI CONTROL BY SIMULATION

In this section, we present the simulation results obtained using MATLAB/Simulink to support the validity of the above theory. A block diagram of the microgrid is shown in Fig.2. The system parameters used for simulation are listed in Table 2. The three-phase inductive local load is 9 kW, 1.5 kVar per phase. The desired voltage at the PCC is equal to the grid voltage. The simulation is performed using Simulink in discrete mode. Table 3 presents the control parameters used in this study. The grid-side impedance is mainly determined by the equivalent impedance of the power transformers and those of the distribution lines. This equivalent impedance is a variable, uncertain value depending on the grid configuration [48]. The variation of this impedance affects the performance of the inverter control, and the gain of the current

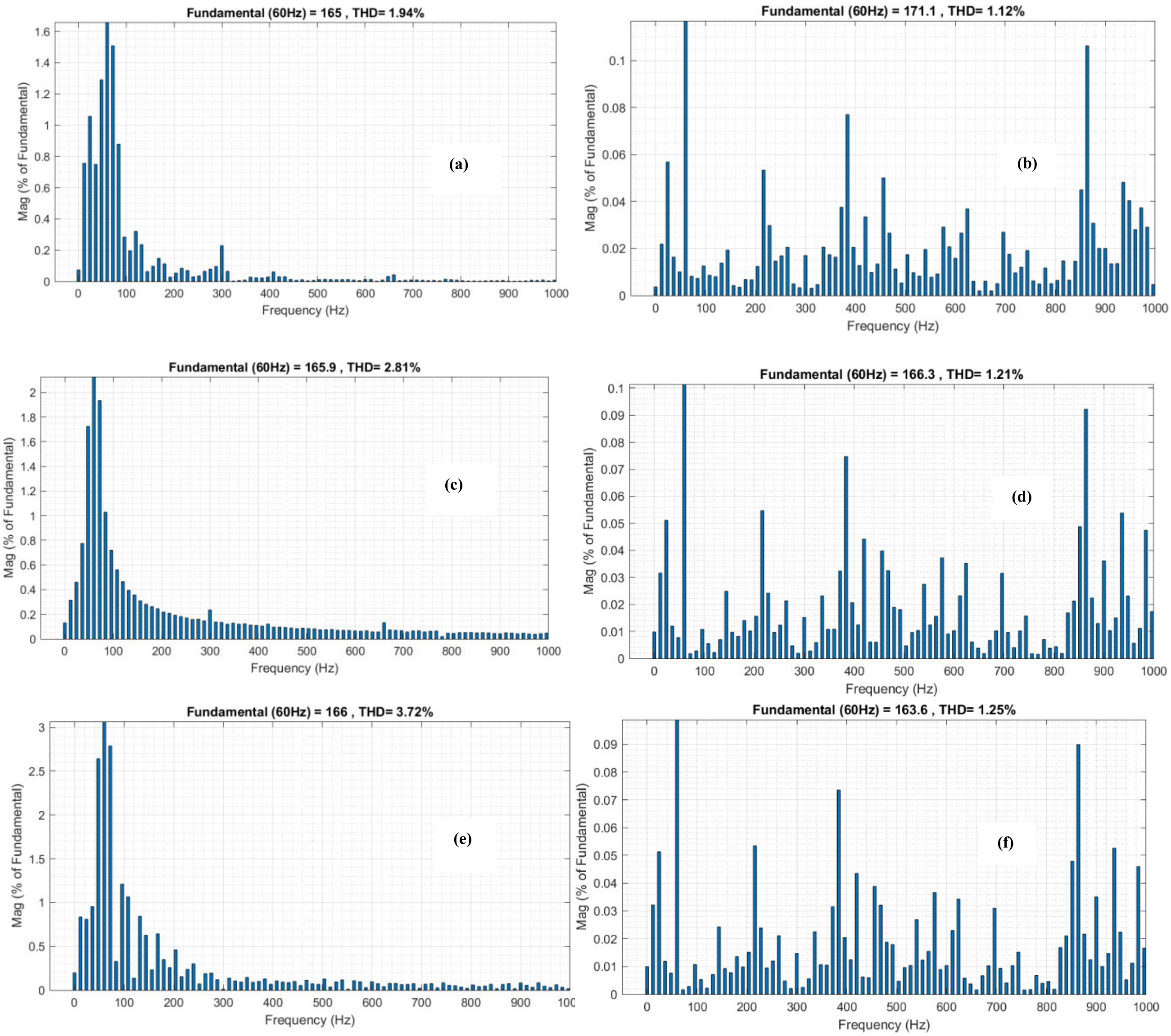

FIGURE 12. PCC voltage THD. (a) and (b) Sc= (9 kW,1.5 kVar). (c) and (d) for Sc=(14 kW, 4 kVar). (e) and (f) for Sc=(11 kW, 2.5 kVar). (a), (c) and (e) with DVI control. (b), (d) and (f) with ADRC control.

loop can be considerably modified, thus leading to a possible harmonic oscillation, or even instability [49]. Therefore, the inverter control must be designed with strong robustness to grid-side impedance variations. Hence the need to test the robustness of the proposed method to grid-side impedance variations [50], [51].

The following section is devoted to verifying the performance of the proposed controller. We compared the simulation results of the proposed ADRC with those of the most deployed droop control (DVI). We consider three disturbances in the system: effect of the variation of the grid-side inductance during connected mode, a sudden variation in load power during islanded mode, and the transition between operating mode.

A. CONNECTED MODE

In this scenario, the microgrid is connected to the grid. We apply the following three values of the grid-side inductance L_G: 10 mH, 4 mH and 100μH.

The total harmonic distortion (THD) of the current injected into the grid i_G under grid-side inductance variation are presented in Fig.7. For better comparison, the steady-state THD values are listed in Table 4.

We notice that the THD values of i_G by the DVI control are greater compared to the THD with the proposed ADRC. The proposed control better suppresses the current ripple and compensates the disturbance due to the variation of L_G which demonstrates the robustness of the ADRC to an internal disturbance.

B. ISLANDED MODE

The main purpose of an islanded mode is to provide backup power to the local load when the main grid is disconnected. In this case, the microgrid has no reference voltage or frequency imposed by the grid and the inverter must be intelligent and act as a grid forming inverter. Which means that the inverter must control the microgrid voltage and maintain the frequency at a stable value and within the limits acceptable by standards [52]. The goal of this scenario is to test the robustness and the ability to reject the disturbance of the controller by varying the load demand.

This disturbance is produced by the connection and sudden disconnection of two other local loads A and B of 4 kW, 1.5 kVar and 2 kW, 1 kVar, respectively.

Let us compare the simulation results of the conventional DVI control with those achieved by the proposed ADRC control. At t = 0.2 s, load A is connected to the PCC and the total demand of the load becomes 13 kW, 3 kVar (Fig.8 and Fig.9).

Around 0.5 s, the load B is added to the demand to have a total power of 15 kW, 4 kVar. When the load A is disconnected around 0.7 s and the load B at 0.95 s, the power demand decreases from 11 kW, 2.5 kVar to 9 kW, 1.5 kVar at t = 0.95 s. We notice that despite the absence of the main grid, the load demand is satisfied with DVI and ADRC.

The proposed ADRC control performs better than DVI because DVI took between 0.1 s and 0.12 s to reach the requested power. However, the active and reactive powers stabilize after only 0.04 s with the ADRC control (Fig.8 and Fig.9). We notice from fig.10 that the PCC voltage amplitude v_c follows its reference throughout the simulation despite the load variation.

Fig.11 shows the system frequency during islanded mode. We note that the ADRC controller stabilizes the frequency at exactly 60 Hz with low overshoot and a very short transient regime during the load variation. In contrast, the conventional DVI controller cannot stabilize the frequency at 60 Hz. It experiences a reduction of up to 0.5% which exceeds acceptable limits, which may cause adverse effects on sensitive loads.

Fig. 12 shows the values of the harmonic distortion rate (THD) of the PCC voltage in islanded mode. When the charging power is 9 kW, 1.5 kVar, the THD is 1.94% with DVI and 1.12% with the proposed ADRC. With increasing load, the THD becomes 2.81% with DVI and 1.21% with ADRC. Similarly, when load A is disconnected, the THD is 3.72% with DVI and 1.25% with ADRC. It is noted that the proposed ADRC control results in lower PCC voltage THD values with better performance and power quality.

Fig.13 presents the waveforms of the total load current, the current injected by the inverter and the grid current. We see that the current injected by the inverter follows exactly the load current throughout the islanded mode and the grid current is zero since the grid is disconnected.

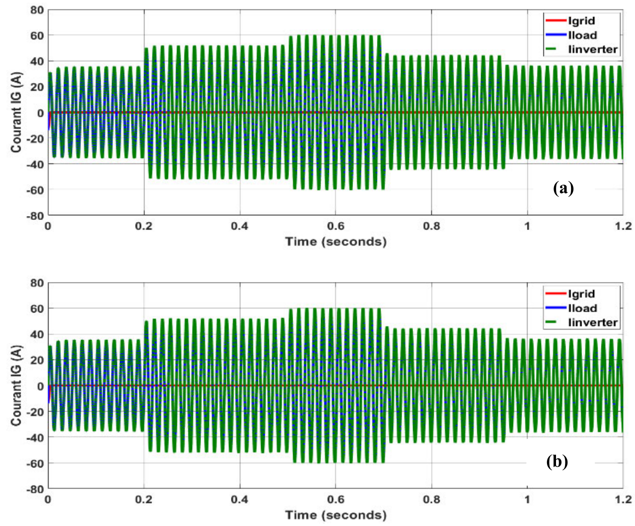

FIGURE 13. Currents waveforms during islanded mode. (a) with DVI control. (b) with ADRC control.

It can be concluded that the microgrid also behaved well in the face of load variations, without any notable transient phenomena. The proposed ADRC controller allows the inverter to function as a voltage source and satisfy the load even in the absence of the main grid with better energy quality. In addition, it has great robustness and strong ability to resist load disturbances.

C. SEAMLESS TRANSITION BETWEEN OPERATING MODES

1) PERFORMANCE VERIFICATION

At the start of the simulation, the grid is operating normally and the microgrid is connected to the grid. Fig.14 shows the waveform of the current injected into the grid. We notice that at t = 0.3 s, the grid disconnects, and the inverter must satisfy the load and ensure control of the voltage and frequency.

The PCC voltage, its first and second derivatives are the control variables. They should follow these corresponding references. The values estimated by the ESO must converge towards their references and the estimation errors tend towards zero.

Fig.15 and Fig.16 illustrate the variation of the active and reactive power of the grid, the load, and that supplied by the inverter during this scenario.

The inductive load begins to increase by 3 kW, 1.5 kVar between 0.5 s and 0.75 s. Despite the variation of the load power, we see that it is satisfied in islanded mode. This justifies the robustness and good energy management of the ADRC control.

The PCC voltage and their first and second derivatives, along with their estimates, are shown in Fig.17. In summary, the observer estimates the voltage and these derivatives well and the control makes it possible to follow the references without any oscillation in transient conditions. The proposed ADRC control method also achieves tracking performance, and the estimation errors almost tend to zero (Fig.18).

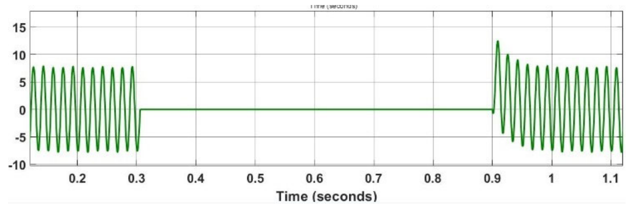

FIGURE 14. Grid current during transition between operating mode.

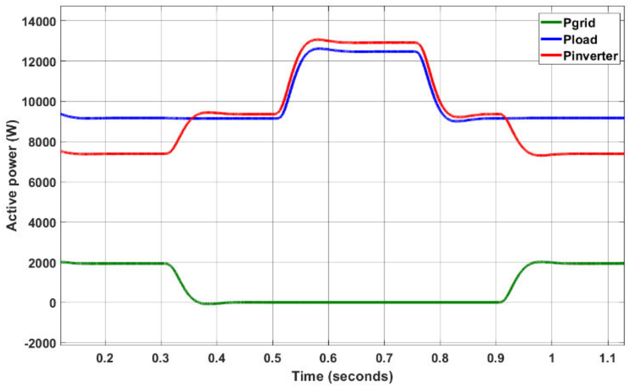

FIGURE 15. Active power variation during simulation.

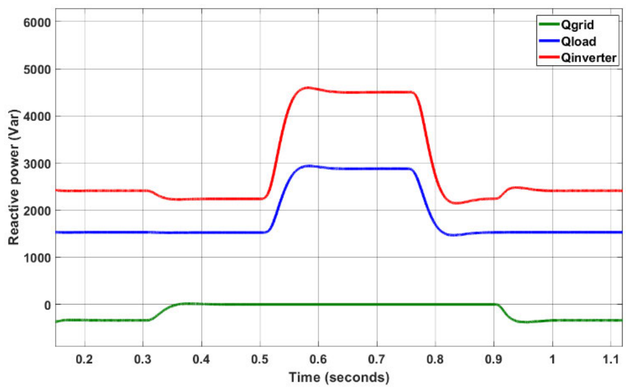

FIGURE 16. Reactive power variation during simulation.

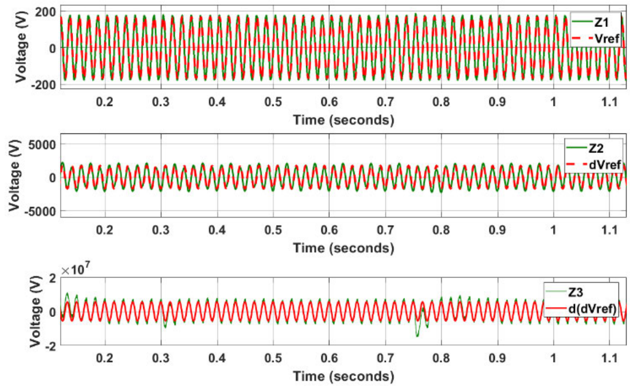

FIGURE 17. State variables and their estimates by ESO.

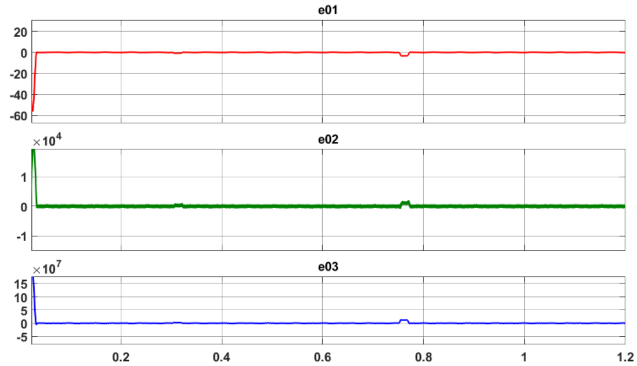

FIGURE 18. Estimation errors with ADRC.

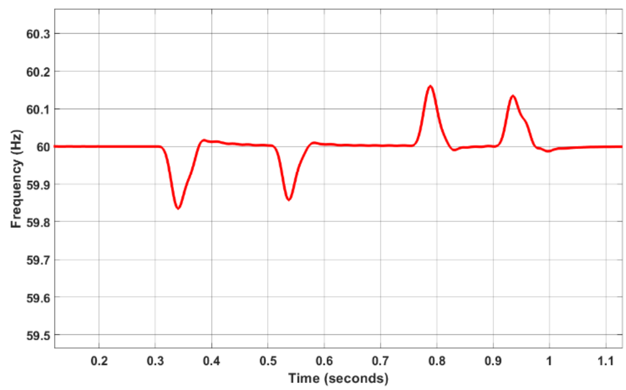

FIGURE 19. Frequency during transition between operating mode.

Fig.19 illustrates the frequency variation during the simulation. We notice that, despite the sudden increase and decrease of the load, the frequency presents a low overshoot with rapid stability around exactly 60 Hz.

Fig.20 shows the magnitude of the PCC voltage. We see that the voltage is very well controlled with the proposed method despite the load variation and the transitions between operating modes.

2) INFLUENCE OF THE GRID-SIDE IMPEDANCE

Simulations are carried out to study the effect of varying grid-side impedance on transitions between operating modes [51]. Initially, the microgrid is connected to the grid with $L_G = 4\ mH$. Islanding occurs around 0.3 s and the grid reconnects at 0.9 s.

Fig.21 presents the PCC and grid voltage amplitudes. In Fig.22, we show the PCC and grid voltage waveforms during transition from connected to islanded mode. We see that both approaches control the voltage which follows its reference. As the grid is reconnected at 0.9 s (Fig.23), a voltage overshoot of 9% is observed with the DVI (zoom of Fig.21). The stable state is reached after 0.04 s.

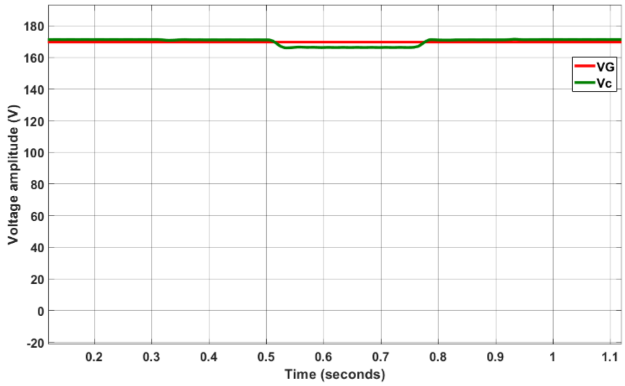

FIGURE 20. Voltage amplitude during transition between operating mode.

From this result, we can understand that the DVI controller helps to reach the steady state after the transition phase, but the response to transients needs to be improved to achieve a faster and non-overshoot response.

The frequency is shown in Fig.24. We see that the DVI control cannot stabilize the frequency at 60 Hz, it dropped around 0.2 Hz during islanded mode. It is set at 59.92 Hz when the grid is reconnected at 0.9 s.

While the proposed ADRC control demonstrates frequency stability at exactly 60 Hz during connected and islanded mode. At times of transition from one mode to another, the frequency undergoes a small and fast oscillation and the ADRC controller observes the disturbance and quickly compensates for it.

To test the impact of the grid-side impedance on the control, we decrease the inductance L_G to 100μH, and we compare the simulation results. Fig.25 and Fig.26 shows the PCC voltage waveforms during transitions from one operating mode to another.

Fig. 27 shows the PCC and grid voltage amplitudes during this study. We see that the transition from connected mode to islanded mode is ensured with DVI and ADRC. But reconnecting the grid at 0.9 s caused a significant voltage drop with DVI.

Due to the low inertia with DVI, the robustness of DVI weakens with the decrease of LG and the frequency suffers a voltage drop of 0.36% in islanded mode (Fig.28 (a)). However, the proposed controller provides more inertia and damping, which helps stabilize the voltage and frequency, as shown in Fig.28 (b).

We concluded that the proposed ADRC control still ensures voltage stability. This validates its robustness even with a low value of L_G.

VI. EXPERIMENTAL VALIDATION

To demonstrate the efficacy and superiority of the control mechanism proposed in this section, specifically to establish a seamless mode transfer from the connected mode to the islanded mode, a real-time simulation is analyzed in this section. The test system is illustrated in Fig.29.

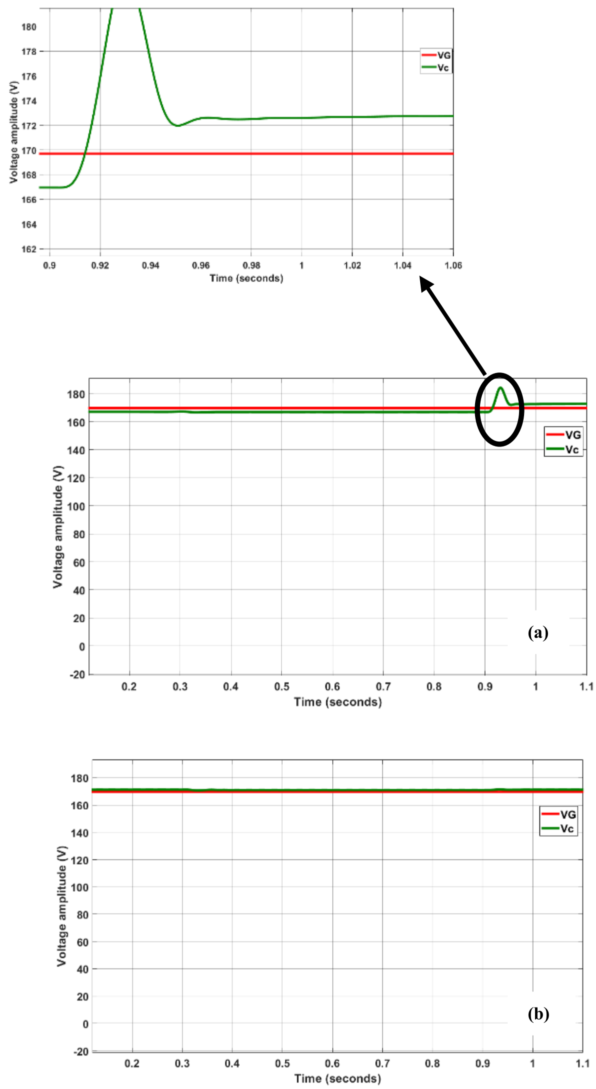

FIGURE 21. Amplitude voltage during transition from one mode to another. (a) with DVI control, (b) with ADRC control.

It mainly includes a digital signal processors (DSP) controller, LabVolt modules [53], a power supply (120 V–60 Hz, three-phase), IGBT Chopper/Inverter (0–20 kHz, 420 Vmax), and a three-phase breaker. The three-phase resistive load available in the laboratory is 80 Ω per phase. The main parameters are listed in Table 5.

Two sensors are used to measure the input signals from v_{inv} and v_G (Fig.30). Since the DSP only receives a positive voltage between 0 and +3.3 V, two voltage step-downs are used to detect and convert the voltages to a low-level signal. To eliminate negative values, we must add two level shifters in cascade. Therefore, the output signals from the two-level shifters are injected to the two Analog-to-Digital Converter (ADC) pins on the kit. Then, the C code generated by the Code

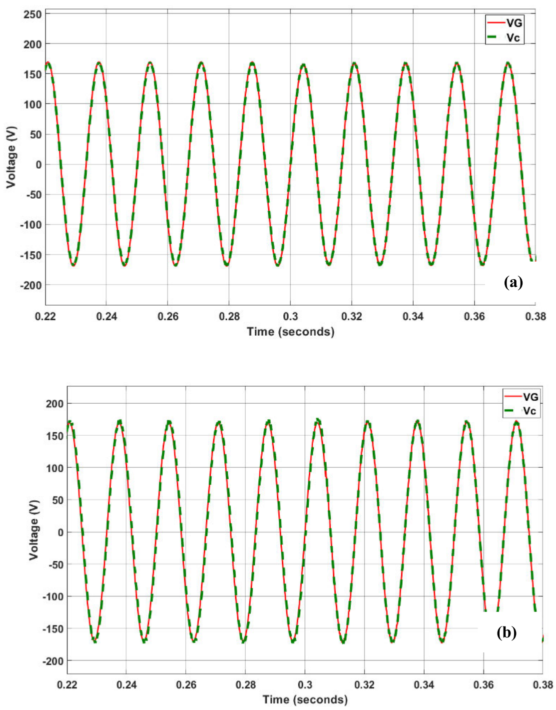

FIGURE 22. PCC voltage waveform during transition from connected to islanded mode. (a) with DVI control, (b) with ADRC control.

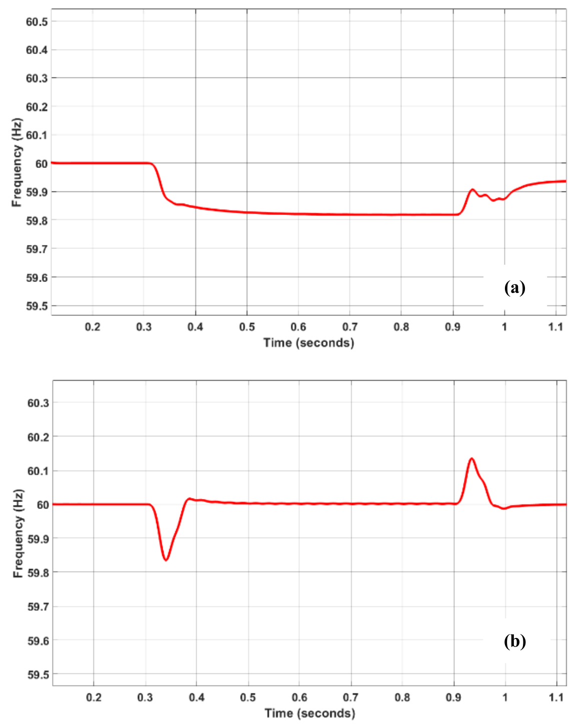

FIGURE 24. Frequency during transition from one mode to another. (a) with DVI control, (b) with ADRC control.

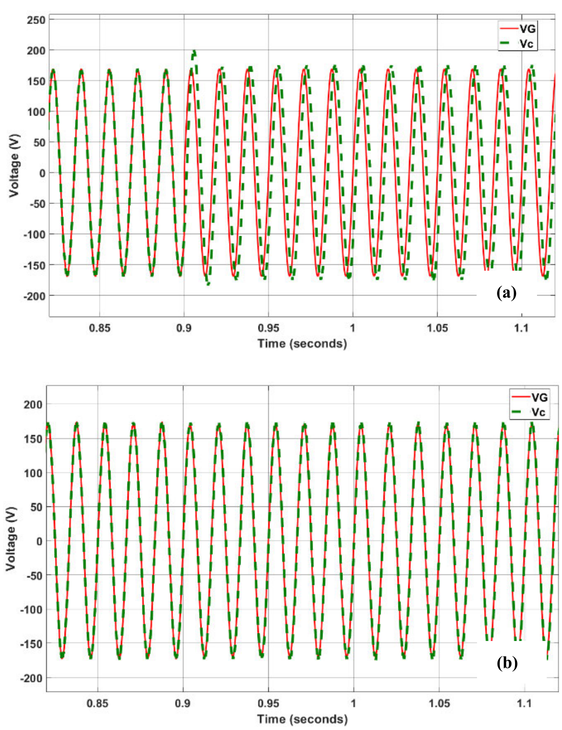

FIGURE 23. PCC voltage waveform during transition from islanded to connected mode. (a) with DVI control, (b) with ADRC control.

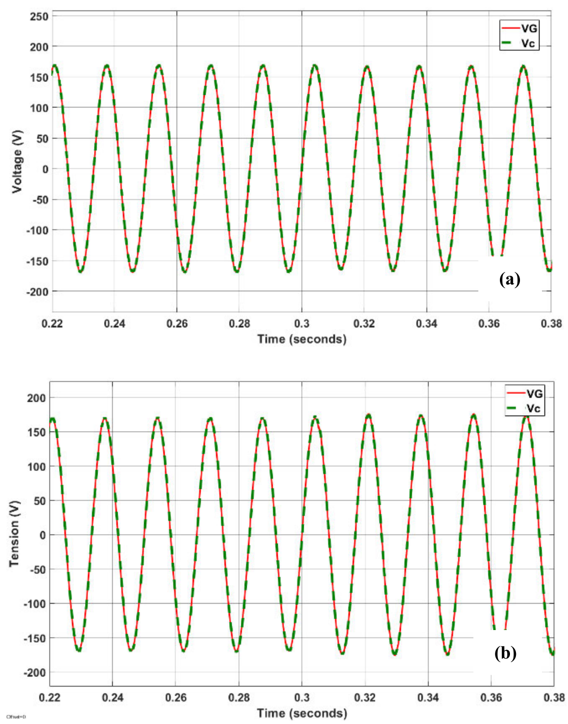

FIGURE 25. Voltage waveform during transition from connected to islanded mode. (a) with DVI control, (b) with ADRC control.

Composition Studio software injects the signals to the ADC blocks in the simulation. Moreover, we must compensate for the shift and the reduction in voltage made by the shifter and the voltage step-down, which is why we added the two compensation gains to the output of each ADC. After that, the

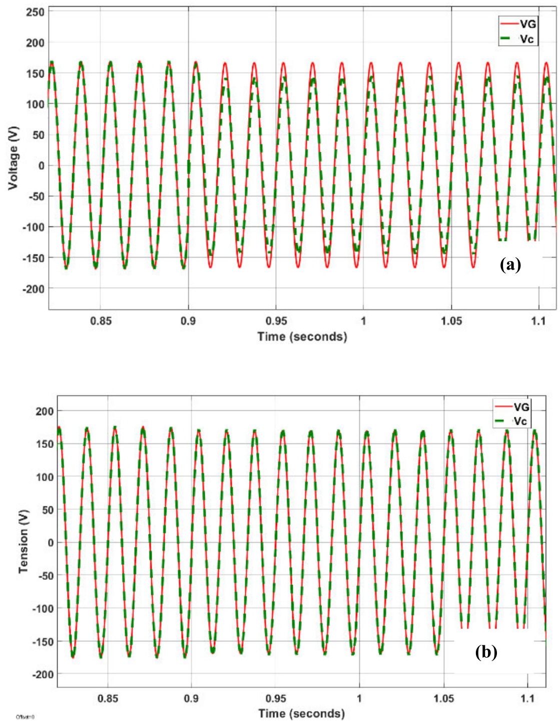

FIGURE 26. PCC voltage waveform during transition from islanded to connected mode. (a) with DVI control, (b) with ADRC control.

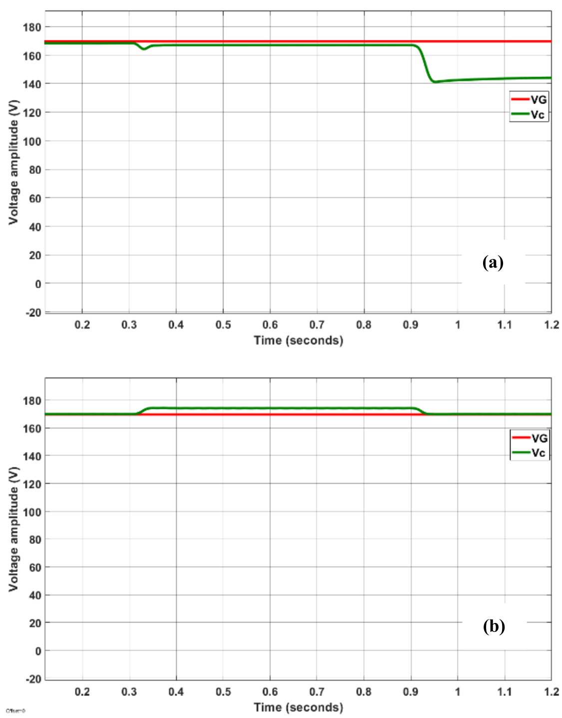

FIGURE 27. Amplitude voltage during transition from one mode to another. (a) with DVI control, (b) with ADRC control.

measured voltage signals v_{inv} and v_G are constructed and used in the ADRC control formula to generate the six pulse signals. Using a DB9 connector, the switching signals are injected to

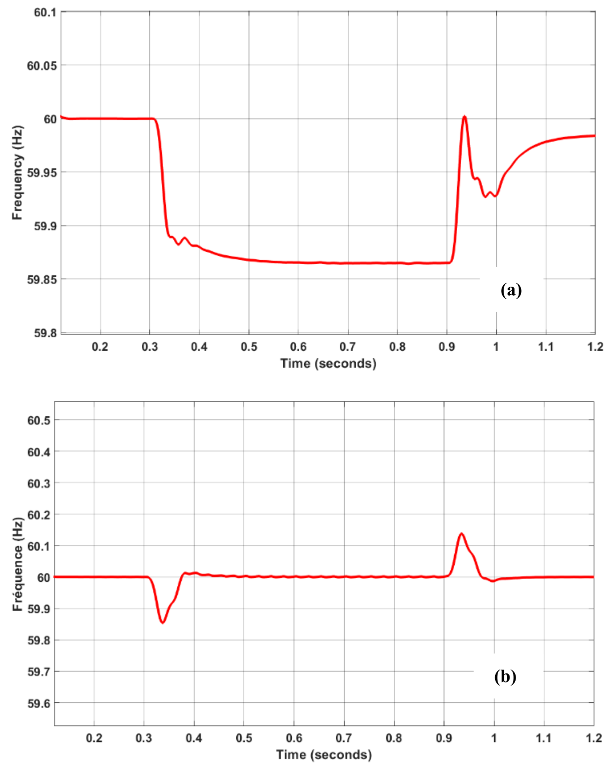

FIGURE 28. Frequency during transition from one mode to another. (a) with DVI control, (b) with ADRC control.

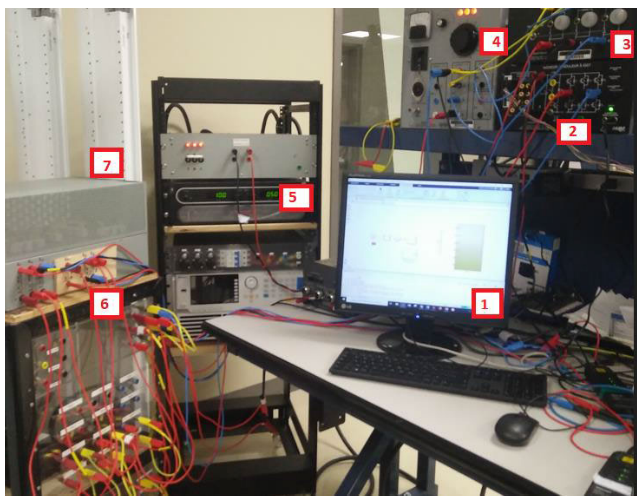

FIGURE 29. Experimental setup. (1) Controller in the computer (i7-2.4GHz). (2) Inverter. (3) Breaker. (4) Main Grid. (5) DC source (6) LCL filter. (7) Load.

control the IGBTs of the Labvolt inverter. A schematic of the processor in the loop controller is shown in Fig.30.

The PCC voltage is detected and measured every 50 μs. This analog signal is digitized and sent to a TMS320F28335 DSP, which produces a control signal and output pulse width modulation (PWM) of 16 kHz. The performance of the proposed controller is investigated in two

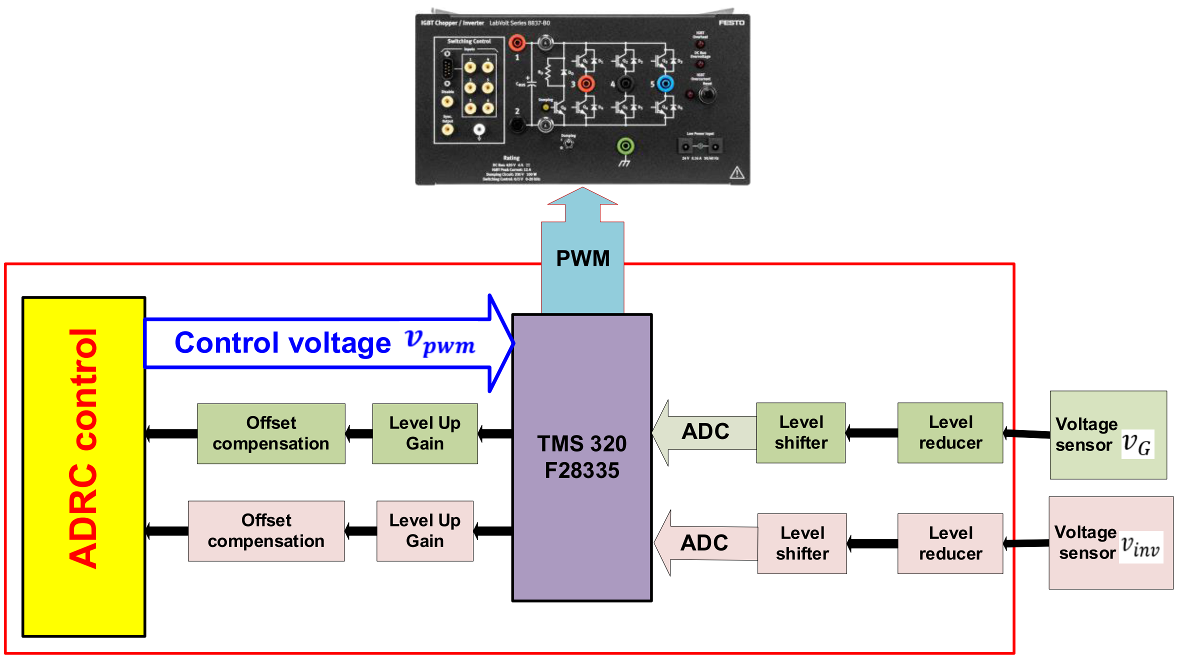

FIGURE 30. **Schematic diagram for the processor in the loop controller validation with TI C2000 DSP.**

TABLE 5. **System parameters used for real-time implementation.**

Description	Value	Unit
DC bus voltage Vdc	100	V
Grid voltage V_G	60	V
Grid-side inductance L_G	20	mH
Grid-side resistance R_G	1	Ω
Inverter-side inductance L	20	mH
Inverter-side resistance R	1	Ω
Capacitance C	90	µF
Frequency f	60	Hz

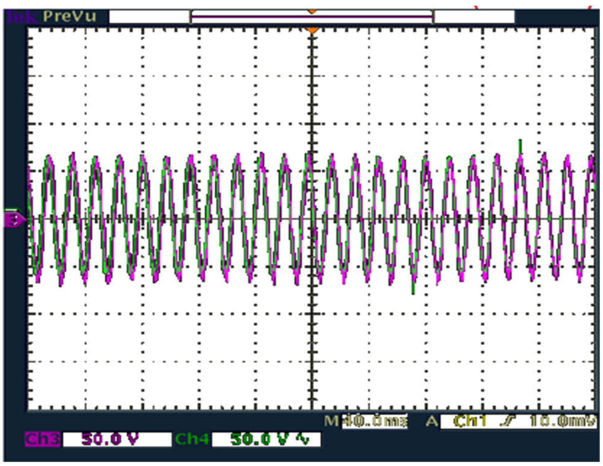

FIGURE 31. **Steady state experimental results of PCC (magenta) and grid (green) voltages waveforms during connected mode.**

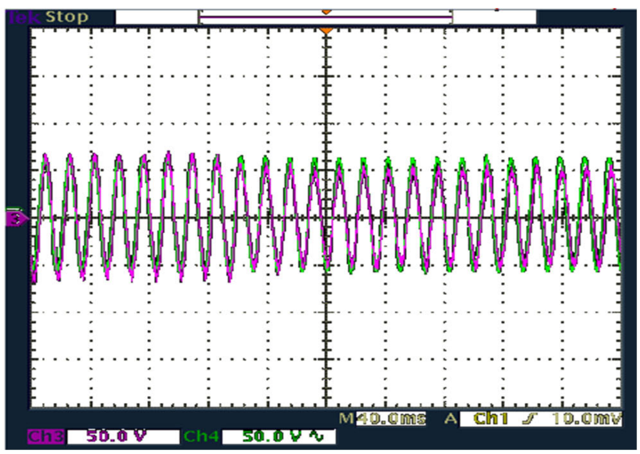

FIGURE 32. **Steady state experimental results of PCC (magenta) and grid (green) voltages waveforms during transition from connected to islanded mode.**

different scenarios: the transition from connected to islanded mode, and vice versa.

The experimental results show the PCC and grid voltages in the connected (Fig.31) and islanded modes (Fig.33).

The PCC and grid voltage waveforms during the transition from connected to islanded mode are shown in Fig.32 and from islanded to connected mode in Fig.34.

It can be clearly observed that the stability of the system is guaranteed, and the microgrid recovers its stable performance in the steady state with a minimum number of transients and no oscillations.

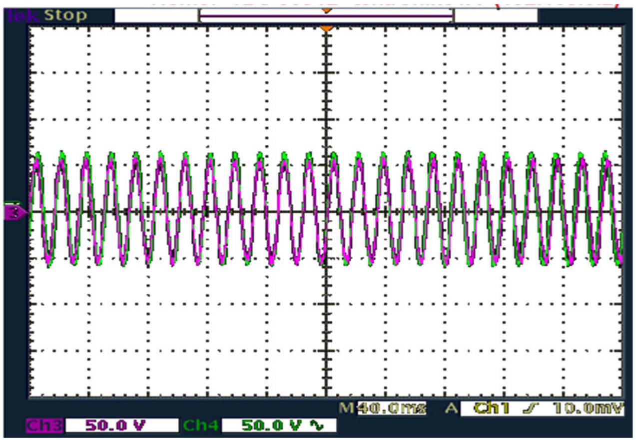

FIGURE 33. Steady state experimental results of PCC (magenta) and grid (green) voltages waveforms during islanded mode.

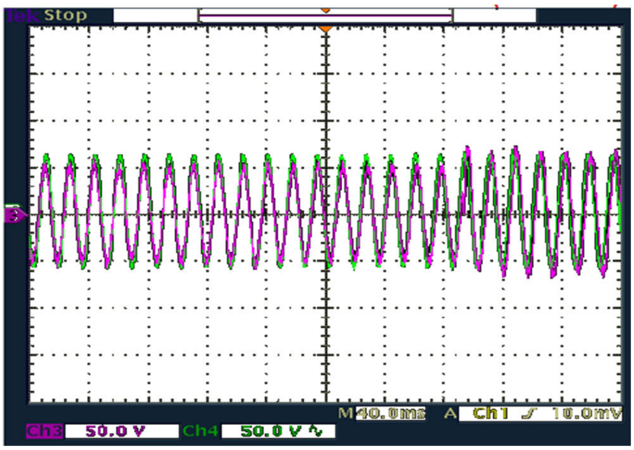

FIGURE 34. Steady state experimental results of PCC (magenta) and grid (green) voltages during transition from islanded to connected mode.

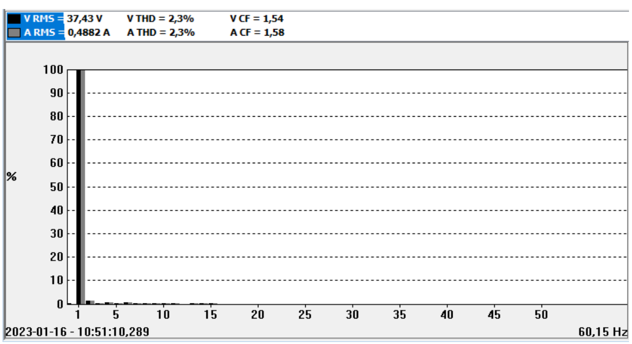

FIGURE 35. Experimental results of PCC voltage and load current THD during islanded mode.

The THD of the PCC voltage and load current during the islanded (Fig.35) and connected modes (Fig.36) are 2.3% and 3.3%, respectively. This proves that the proposed method makes it possible to obtain less distortion, and therefore, a better THD.

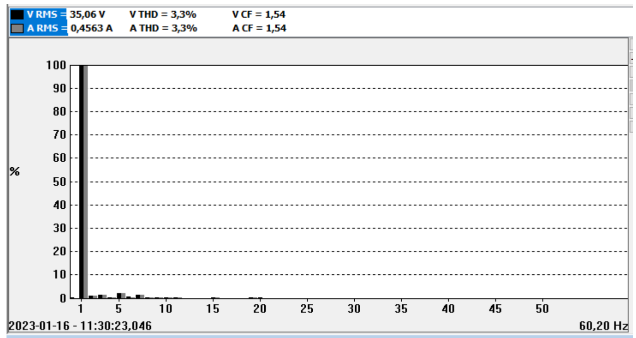

FIGURE 36. Experimental results of PCC voltage and load current THD in connected mode.

VII. CONCLUSION

In this study, an ARDC command is designed for a three-phase microgrid inverter. The proposed strategy is compared with a conventional DVI strategy. The theoretical analysis is validated by simulations and experimental results. The experimental results obtained using the laboratory prototype confirmed the following:

- The controller allows the inverter to operate as a voltage source in the islanded mode and as a current source in the connected mode with better power quality, thereby verifying the effectiveness and feasibility of the ADRC implementation.
- It provides excellent performance with the same control structure in both the grid-connected and isolated modes. Moreover, the flexibility of the transition with the proposed method is ensured without an islanding detection algorithm or PLL with fewer measurement sensors. These characteristics increase the reliability and robustness of a system.
- The proposed controller offers more inertia and damping, which helps stabilize the voltage and frequency in all operating modes.
- The experimental validation of the proposed method demonstrated that a real-time implementation using a standard DSP is easy to achieve.
- Simulation results show that the proposed control improves the speed, robustness, and stability of the microgrid and is superior to DVI control.
- Excellent voltage and frequency regulation in islanded mode within a limited range, even during unintentional power grid failure.
- High robustness when changing the load during islanded mode and changing the grid-side impedance during connected mode.
- The stability of the ADRC is analyzed, which shows that it can remain stable under large variations in ω_0 and ω_c.

In the future, this research could be extended to storage batteries, photovoltaic panels and non-linear charging. Moreover, in a microgrid with several distributed generators it would be important to analyze and ensure better energy management between several inverters in parallel. The study of electric vehicle charging is a remarkable topic that deserves further research using the proposed ADRC control method.

REFERENCES

[1] B. Kroposki, B. Johnson, Y. Zhang, V. Gevorgian, P. Denholm, B.-M. Hodge, and B. Hannegan, "Achieving a 100% renewable grid: Operating electric power systems with extremely high levels of variable renewable energy," *IEEE Power Energy Mag.*, vol. 15, no. 2, pp. 61–73, Mar. 2017.

[2] P. Peltoniemi, "Compensating the rotating mass kinetic energy in grids including high shares of renewable," in *Proc. 19th Eur. Conf. Power Electron. Appl. (EPE ECCE Europe)*, Warsaw, Poland, Sep. 2017, pp. P.1–P.10.

[3] F. Milano, F. Dörfler, G. Hug, D. J. Hill, and G. Verbič, "Foundations and challenges of low-inertia systems," in *Proc. Power Syst. Comput. Conf. (PSCC)*, Jun. 2018, pp. 1–25.

[4] B. K. Poolla, S. Bolognani, and F. Dörfler, "Optimal placement of virtual inertia in power grids," *IEEE Trans. Autom. Control*, vol. 62, no. 12, pp. 6209–6220, Dec. 2017.

[5] J. Hu, R. Harmsen, W. Crijns-Graus, E. Worrell, and M. van den Broek, "Identifying barriers to large-scale integration of variable renewable electricity into the electricity market: A literature review of market design," *Renew. Sustain. Energy Rev.*, vol. 81, pp. 2181–2195, Jan. 2018.

[6] S. R. Kumar, F. Gafaro, A. Daka, and A. Raturi, "Modelling and analysis of grid integration for high shares of solar PV in small isolated systems—A case of kiribati," *Renew. Energy*, vol. 108, pp. 589–597, Aug. 2017.

[7] M. Haque and P. Wolfs, "A review of high PV penetrations in LV distribution networks: Present status, impacts and mitigation measures," *Renew. Sustain. Energy Rev.*, vol. 62, pp. 1195–1208, Sep. 2016.

[8] M. F. M. Arani and E. F. El-Saadany, "Implementing virtual inertia in DFIG-based wind power generation," *IEEE Trans. Power Syst.*, vol. 28, no. 2, pp. 1373–1384, May 2013.

[9] J. Matevosyan, B. Badrzadeh, T. Prevost, E. Quitmann, D. Ramasubramanian, H. Urdal, S. Achilles, J. MacDowell, S. H. Huang, V. Vital, J. O'Sullivan, and R. Quint, "Grid-forming inverters: Are they the key for high renewable penetration?" *IEEE Power Energy Mag.*, vol. 17, no. 6, pp. 89–98, Nov. 2019.

[10] M. Ganjian-Aboukheili, M. Shahabi, Q. Shafiee, and J. M. Guerrero, "Seamless transition of microgrids operation from grid-connected to islanded mode," *IEEE Trans. Smart Grid*, vol. 11, no. 3, pp. 2106–2114, May 2020.

[11] Z. Guo, D. Sha, and X. Liao, "Voltage magnitude and frequency control of three-phase voltage source inverter for seamless transfer," *IET Power Electron.*, vol. 7, no. 1, pp. 200–208, Jan. 2014.

[12] G. G. Talapur, H. M. Suryawanshi, L. Xu, and A. B. Shitole, "A reliable microgrid with seamless transition between grid connected and islanded mode for residential community with enhanced power quality," *IEEE Trans. Ind. Appl.*, vol. 54, no. 5, pp. 5246–5255, Sep. 2018.

[13] P. Sun, H. Xu, J. Yao, Y. Chi, S. Huang, and J. Cao, "Dynamic interaction analysis and damping control strategy of hybrid system with grid-forming and grid-following control modes," *IEEE Trans. Energy Convers.*, vol. 38, no. 3, pp. 1639–1649, Sep. 2023.

[14] K. Jia, H. Wei, T. Bi, D. W. P. Thomas, and M. Sumner, "An islanding detection method for multi-DG systems based on high-frequency impedance estimation," *IEEE Trans. Sustain. Energy*, vol. 8, no. 1, pp. 74–83, Jan. 2017.

[15] S. Chakraborty, S. Patel, G. Saraswat, A. Maqsood, and M. V. Salapaka, "Seamless transition of critical infrastructures using droop controlled grid-forming inverters," *IEEE Trans. Ind. Electron.*, vol. 71, no. 2, pp. 1535–1546, Feb. 2024.

[16] A. Alsaif, Z. Miao, and L. Fan, "Comparison of islanding and synchronization for a microgrid with different converter control," in *Proc. North Amer. Power Symp. (NAPS)*, Wichita, KS, USA, Oct. 2019, pp. 1–6.

[17] H. Zheng, Z. Liu, R. An, J. Liu, T. Wu, and Z. Lin, "An islanding detection method using synchronized small-AC-signal injection for grid-forming inverters in microgrids," *IEEE Trans. Power Electron.*, vol. 38, no. 5, pp. 5816–5831, May 2023.

[18] P. Utkarsha and N. K. S. Naidu, "Seamless transfer of virtual synchronous generator using virtual synchronizing torque controller," *Int. J. Circuit Theory Appl.*, pp. 4488–4497, 2024.

[19] F. Yao, J. Zhao, X. Li, L. Mao, and K. Qu, "RBF neural network based virtual synchronous generator control with improved frequency stability," *IEEE Trans. Ind. Informat.*, vol. 17, no. 6, pp. 4014–4024, Jun. 2021.

[20] P. Buduma, M. K. Das, R. T. Naayagi, S. Mishra, and G. Panda, "Seamless operation of master–slave organized AC microgrid with robust control, islanding detection, and grid synchronization," *IEEE Trans. Ind. Appl.*, vol. 58, no. 5, pp. 6724–6738, Sep. 2022.

[21] Z. Li, Z. Cheng, S. Li, J. Si, J. Gao, W. Dong, and H. S. Das, "Virtual synchronous generator and SMC-based cascaded control for voltage-source grid-supporting inverters," *IEEE J. Emerg. Sel. Topics Power Electron.*, vol. 10, no. 3, pp. 2722–2736, Jun. 2022.

[22] M. C. Chandorkar, D. M. Divan, and R. Adapa, "Control of parallel connected inverters in standalone AC supply systems," *IEEE Trans. Ind. Appl.*, vol. 29, no. 1, pp. 136–143, Feb. 1993.

[23] S. Chakraborty, J. Park, G. Saraswat, T. Meyers, J. Wang, S. Tiwari, V. Khatana, A. Maqsood, A. Somani, and M. V. Salapaka, "Emergency power supply system for critical infrastructures: Design and large scale hardware demonstration," *IEEE Access*, vol. 11, pp. 114509–114526, 2023.

[24] U. B. Tayab, M. A. B. Roslan, L. J. Hwai, and M. Kashif, "A review of droop control techniques for microgrid," *Renew. Sustain. Energy Rev.*, vol. 76, pp. 717–727, Sep. 2017.

[25] H. P. Beck and R. Hesse, "Virtual synchronous machine," in *Proc. 9th Int. Conf. Elect. Power Quality Utilisation*, Barcelona, Spain, Oct. 2007, pp. 1–16.

[26] X. Meng, J. Liu, and Z. Liu, "A generalized droop control for grid-supporting inverter based on comparison between traditional droop control and virtual synchronous generator control," *IEEE Trans. Power Electron.*, vol. 34, no. 6, pp. 5416–5438, Jun. 2019.

[27] C. Glöckler, D. Duckwitz, and F. Welck, "Virtual synchronous machine control with virtual resistor for enhanced short circuit capability," in *Proc. IEEE PES Innov. Smart Grid Technol. Conf. Eur. (ISGT-Europe)*, Turin, Italy, Sep. 2017, pp. 1–6.

[28] X. Meng, Z. Liu, H. Zheng, and J. Liu, "A universal controller under different operating states for parallel inverters with seamless transfer capability," *IEEE Trans. Power Electron.*, vol. 35, no. 9, pp. 9794–9812, Sep. 2020.

[29] H. Ahmed, S. Biricik, and M. Benbouzid, "Linear Kalman filter-based grid synchronization technique: An alternative implementation," *IEEE Trans. Ind. Informat.*, vol. 17, no. 6, pp. 3847–3856, Jun. 2021.

[30] B. C. Babu, K. Sridharan, E. Rosolowski, and Z. Leonowicz, "Analysis of SDFT based phase detection system for grid synchronization of distributed generation systems," *Eng. Sci. Technol., Int. J.*, vol. 17, no. 4, pp. 270–278, 2014.

[31] M. A. Perez, J. R. Espinoza, L. A. Moran, M. A. Torres, and E. A. Araya, "A robust phase-locked loop algorithm to synchronize static-power converters with polluted AC systems," *IEEE Trans. Ind. Electron.*, vol. 55, no. 5, pp. 2185–2192, May 2008.

[32] A. Bouknadel, N. Ikken, A. Haddou, N.-E. Tariba, H. E. Omari, and H. E. Omari, "A new SOGI-PLL method based on fuzzy logic for grid connected PV inverter," *Int. J. Elect. Comput. Eng.*, vol. 9, no. 4, pp. 2264–2273, 2019.

[33] X. Du, Y. Liu, G. Wang, P. Sun, H.-M. Tai, and L. Zhou, "Three-phase grid voltage synchronization using sinusoidal amplitude integrator in synchronous reference frame," *Int. J. Electr. Power Energy Syst.*, vol. 64, pp. 861–872, Jan. 2015.

[34] N. F. Guerrero-Rodríguez, A. B. Rey-Boué, L. C. Herrero-de Lucas, and F. Martinez-Rodrigo, "Control and synchronization algorithms for a grid-connected photovoltaic system under harmonic distortions, frequency variations and unbalances," *Renew. Energy*, vol. 80, pp. 380–395, Aug. 2015.

[35] Y. F. Wang and Y. W. Li, "Three-phase cascaded delayed signal cancellation PLL for fast selective harmonic detection," *IEEE Trans. Ind. Electron.*, vol. 60, no. 4, pp. 1452–1463, Apr. 2013.

[36] H. R. Baghaee, D. Mlakic, S. Nikolovski, and T. Dragicevic, "Support vector machine-based islanding and grid fault detection in active distribution networks," *IEEE J. Emerg. Sel. Topics Power Electron.*, vol. 8, no. 3, pp. 2385–2403, Sep. 2020.

[37] P. Das, S. Ghore, and M. Biswal, "Comparative assessment of various islanding detection methods for AC and DC microgrid," in *Proc. 1st Int. Conf. Power, Control Comput. Technol. (ICPC2T)*, Raipur, India, Jan. 2020, pp. 396–400.

[38] S. Golestan, J. M. Guerrero, and J. C. Vasquez, "Three-phase PLLs: A review of recent advances," *IEEE Trans. Power Electron.*, vol. 32, no. 3, pp. 1894–1907, Mar. 2017.
[39] Z. Ali, N. Christofides, L. Hadjidemetriou, E. Kyriakides, Y. Yang, and F. Blaabjerg, "Three-phase phase-locked loop synchronization algorithms for grid-connected renewable energy systems: A review," *Renew. Sustain. Energy Rev.*, vol. 90, pp. 434–452, Jul. 2018.
[40] T. Meyers and B. Mather, "Time disciplined non-PLL active synchronization for grid forming inverters," in *Proc. IEEE Texas Power Energy Conf. (TPEC)*, College Station, TX, USA, Feb. 2021, pp. 1–6.
[41] J. Han, "From PID to active disturbance rejection control," *IEEE Trans. Ind. Electron.*, vol. 56, no. 3, pp. 900–906, Mar. 2009.
[42] Z.-G. Su, L. Sun, W. Xue, and K. Y. Lee, "A review on active disturbance rejection control of power generation systems: Fundamentals, tunings and practices," *Control Eng. Pract.*, vol. 141, Dec. 2023, Art. no. 105716.
[43] B. Wang, Z. Shen, H. Liu, and J. Hu, "Linear ADRC direct current control of grid-connected inverter with LCL filter for both active damping and grid voltage induced current distortion suppression," *IET Power Electron.*, vol. 11, no. 11, pp. 1748–1755, Sep. 2018.
[44] H. Zhang, J. Xian, J. Shi, S. Wu, and Z. Ma, "High performance decoupling current control by linear extended state observer for three-phase grid-connected inverter with an LCL filter," *IEEE Access*, vol. 8, pp. 13119–13127, 2020.
[45] H. Li, J. Hu, Z. Li, and J. Lu, "Smooth switching control strategy for grid-connected and islanding mode of microgrid based on linear active disturbance rejection controller," in *Proc. 13th IEEE Conf. Ind. Electron. Appl. (ICIEA)*, Wuhan, China, May 2018, pp. 2578–2583.
[46] Z. Gao, "Scaling and bandwidth-parameterization based controller tuning," in *Proc. Amer. Control Conf.*, Denver, CO, USA, vol. 6, Jun. 2003, pp. 4989–4996.
[47] H. Hu, S. Xiao, and H. Shen, "Modified linear active disturbance rejection control for uncertain robot manipulator trajectory tracking," *Math. Problems Eng.*, vol. 13, no. 12, 2021, Art. no. 8892032.
[48] S. Cobreces, E. Bueno, F. J. Rodriguez, F. Huerta, and P. Rodriguez, "Influence analysis of the effects of an inductive-resistive weak grid over L and LCL filter current hysteresis controllers," in *Proc. Eur. Conf. Power Electron. Appl.*, Sep. 2007, pp. 1–10.
[49] J. Sun, "Impedance-based stability criterion for grid-connected inverters," *IEEE Trans. Power Electron.*, vol. 26, no. 11, pp. 3075–3078, Nov. 2011.
[50] H. S. Das, S. Li, B. Lu, and J. Wang, "Virtual dynamic grid impedance and its impacts on harmonics and stability of inverter based resources plant," *IEEE Trans. Power Electron.*, vol. 37, no. 12, pp. 15469–15481, Dec. 2022.
[51] T. Yin, Y. Wang, B. Yue, P. Xu, P. Li, N. Mei, and D. Xu, "Impedance-based stability analysis and stabilization control strategy of MMC-HVDC considering complete control loops," *IEEE Access*, vol. 8, pp. 142900–142915, 2020.
[52] *IEEE Standard for Interconnection and Interoperability of Distributed Energy Resources With Associated Electric Power Systems Interfaces*, IEEE Standard 1547-2018, 2018.
[53] LabVolt Series by Festo Didactic. (2020). *LabVolt Series Equipment*. Accessed: Mar. 2022. [Online]. Available: https://www.labvolt.com

N. YALAOUI (Member, IEEE) received the M.Sc. degree in electrical engineering from École Polytechnique de Montréal, Montreal, QC, Canada, in 2017. She is currently pursuing the Ph.D. degree in power electrical engineering with École de Technologies Supérieure (ÉTS), Université du Québec, Montreal. Her research interests include active disturbance rejection control techniques, control methods for power electronics converters in microgrids, and the seamless transition of microgrid operation.

L. DESSAINT (Life Fellow, IEEE) received the B.Ing., M.Sc.A., and Ph.D. degrees in electrical engineering from École Polytechnique de Montréal, Montreal, QC, Canada, in 1978, 1980, and 1985, respectively.

He is currently a Professor with École de Technologie Supérieure, Université du Québec, Montreal. He held the Hydro-Quebec/Trans Energie Chair on Simulation and Control of Power Systems, from 2001 to 2011, and the ETS Chair on Security of Power Systems, from 2014 to 2017. He is the author of the MathWorks "Sim Power Systems" (SPS) Blockset. He was an Associate Editor of IEEE Transactions on Control Systems Technology, from 2009 to 2013, and *IET Generation, Transmission and Distribution*, from 2015 to 2018. He is an Emeritus Fellow of the Canadian Academy of Engineering and a member of the Cercle d'excellence de l'Université du Québec.

M. REZA DEHBOZORGI received the Ph.D. degree in electrical and computer engineering from the University of New Brunswick, Fredericton, NB, Canada, in 2000, for his work on improving electrical power systems reliability through locally controlled curtailable loads.

He is currently a Research Associate with École de Technologie Supérieure (ÉTS), Montreal, QC, Canada. His research interests include the development of state-of-the-art power electronics devices, renewable energy, high-power high-frequency inverters, power ground power unit (GPU) 3 phase 400 Hz, and battery chargers (SMPS). His research has been applied in the design of magnetic devices and intelligent controllers for capacitance contactors.

K. AL-HADDAD (Life Fellow, IEEE) received the B.Sc. and M.Sc. degrees from the Université du Québec à Trois-Rivières, Canada, in 1982 and 1984, respectively, and the Ph.D. degree from the Institute of National Polytechnique, Toulouse, France, in 1988. Since June 1990, he has been a Professor with the Department of Electrical Engineering, École de Technologie Supérieure (ÉTS), Montreal, QC, Canada, where he has been the holder of the Senior Canada Research Chair in Electric Energy Conversion and Power Electronics, since 2002. He is also a Consultant and has established a solid link with many Canadian and international industries in the fields of power electronics, electric transportation, aeronautics, and telecommunications. He has successfully transferred and implemented dozens of technologies to Canadian and international companies. His research interests include highly efficient static power converters, harmonics, and reactive power control using hybrid filters, voltage-level multipliers, and resonant and multilevel converters, including the modeling, control, and development of prototypes for various industrial applications in electric traction, renewable energy, power supplies for drives, and telecommunications. He is a member of the Academy of Sciences and a fellow of the Royal Society of Canada and the Canadian Academy of Engineering. He was a recipient of the 2014 IEEE IES Dr.-Ing. Eugene Mittelmann Achievement Award. He was elected as the IEEE 2022 Division VI Director. He is the IEEE IES President 2016–2017, an Associate Editor of IEEE Transactions on Industrial Informatics, and an IES Distinguished Lecturer.